RAREFIED PLUME MODELING FOR VISORS MISSION

by

Ann Marie Karis

A Thesis

Submitted to the Faculty of Purdue University

In Partial Fulfillment of the Requirements for the degree of

Master of Science in Aeronautics and Astronautics

School of Aeronautics and Astronautics

West Lafayette, Indiana

May 2022

THE PURDUE UNIVERSITY GRADUATE SCHOOL
STATEMENT OF COMMITTEE APPROVAL

Dr. Alina A. Alexeenko, Chair

School of Aeronautics and Astronautics

Dr. Tom Shih

School of Aeronautics and Astronautics

Dr. Aaron Morris

School of Aeronautics and Astronautics

Approved by:

Dr. Gregory Blaisdell

I would like to dedicate this thesis to my loving partner, Shelby.
Thank you for encouraging me to "dare greatly."

"It is not the critic who counts; not the man who points out how the strong man stumbles, or where the doer of deeds could have done them better. The credit belongs to the man who is actually in the arena, whose face is marred by dust and sweat and blood; who strives valiantly; who errs, who comes short again and again, because there is no effort without error and shortcoming; but who does actually strive to do the deeds; who knows great enthusiasms, the great devotions; who spends himself in a worthy cause; who at the best knows in the end the triumph of high achievement, and who at the worst, if he fails, at least fails while daring greatly, so that his place shall never be with those cold and timid souls who neither know victory nor defeat."

—Theodore Roosevelt

ACKNOWLEDGMENTS

I would like to acknowledge Professor Alexeenko for mentoring and supporting me these past three years. I started out with absolutely no experience in the software used in this thesis and minimal experience in research, but she still believed in me and accepted me as a graduate research assistant in her lab. Professor Alexeenko also guided me through the application process for the NSF GRFP. Without her help, I would have never won the fellowship. I was very low in confidence entering Purdue University because I was denied from every other PhD program to which I applied. Purdue University and Professor Alexeenko took a chance on me, and for that I am eternally grateful.

I also would like to acknowledge Dr. Petr Kazarin. I would not know how to be a researcher , use the software I now know, or know how to present my work in a technical manner without his help. He was always there to mentor me and guide me with patience. He is a mentor and my friend.

Lastly, I would like to thank Professor Shih and Sabina Nketia, a graduate researcher working under Professor Shih at Purdue University. Professor Shih taught me the fundamentals behind Computational Fluid Dynamics (CFD) and has been a constant source of encouragement during the process of learning how to use Fluent as well as setting up my simulation properly. While struggling with meshing, he connected me with Sabina Nketia to teach me how to make a structured mesh. I am grateful for the assistance and guidance.

TABLE OF CONTENTS

LIST OF TABLES

LIST OF FIGURES

ABSTRACT

The Virtual Super-resolution Optics with Reconfigurable Swarms (VISORS) mission aims to produce high-resolution images of solar release sites in the solar corona using a distributed telescope. The collected data will be used to investigate the existence of underlying energy release mechanisms [1]. The VISORS telescope is composed of two spacecraft flying in a formation configuration. The optics spacecraft (OSC) hosts the optic system, while the detector spacecraft (DSC) is located behind the OSC in alignment with the Sun and houses a detector. The two modes of operation for the CubeSats are Science Operations Mode and Standby Mode.

In Science Operations Mode, the two spacecraft are at a close distance which may make the plume impingement an issue. The cold gas thruster propulsion systems in both the OSC and DSC use R-236fa (HFC) refrigerant. The plume from the system is modeled using SPARTA Direct Simulation Monte Carlo (DSMC) Simulator while the refrigerant itself is modeled using an equivalent particle that closely matches viscosity and specific heat [2]. This work aims to investigate plume propagation for two different flow inputs. The DSMC simulations are performed with the input parameters acquired using the isentropic relations and CFD simulations of the 2D axisymmetric nozzle flow. Additionally, the DSMC results are compared to the Boynton-Simons, Roberts-South, and Gerasimov analytical plume models [3]-[14].

The uniform (isentropic-based) and non-uniform (CFD-based) inputs and the resulting plumes were compared, and differences were observed. These differences resulted from non-isentropic behavior of the flow in the nozzle obtained from the CFD simulation. The influence from the nozzle walls was found to be substantial enough to not be ignored. Additionally, it was found that the way a DSMC input is acquired makes a difference when comparing the resulting DSMC plume to the analytical model plume. From the DSMC plume simulations, the Gerasimov model matched the best for the non-uniform, CFD-based input. This is because its assumptions of a supersonic, ideal gas plume were easily met.

1. INTRODUCTION

The objective of Virtual Super-resolution Optics with Reconfigurable Swarms (VISORS) mission is to produce high-resolution images of solar release sites in the solar corona for intervals of 10 seconds using a distributed telescope. The main inquiry of the mission is: "How magnetic reconnection works and operates in the solar atmosphere, within the solar wind, at the dayside magnetopause, and in the magnetotail to initiate and facilitate energy transfer between the different regions of the space environment [1]."

The mission is composed of two spacecraft flying in a formation configuration. The spacecraft in question are two 6U CubeSats with dimensions 30 cm x 20 cm x 10 cm each. The leading CubeSat is an optics spacecraft (OSC) that houses both a sunshade and photon sieve, while the other trailing CubeSat is the detector spacecraft (DSC) which houses an extreme ultraviolet camera. This novel camera gathers coronal images at a high-resolution using diffractive-based imaging technology [1].

As for technology on-board, an orbit maneuver planner utilizes GNSS carrier-phase-phase-phase measurements, and a newly conceived inter-satellite crosslink system is also utilized. The propulsion system is 3 degrees of freedom with the fuel of choice being hexafluoropropane, $C_3H_2F_6$ or HFC-236fa. This technological setup helps avoid collisions and monitors the positions of the cubesats consistently which is critical to the success of the mission. A mission overview can be seen in Figure 1b.

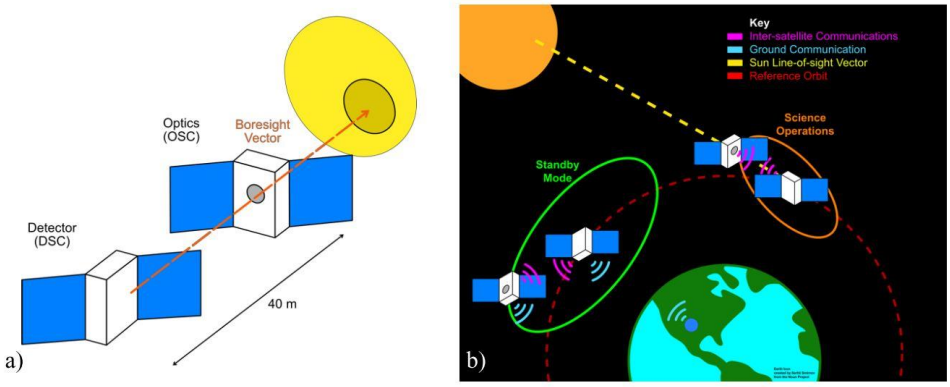

Figure 1: a) OSC and DSC Science Formation with Sun b) VISORS Modes [1]

1.1 Motivation

The two modes of operation for the cubesats are Science Operations Mode and Standby Mode. The two spacecraft will be in the alignment 40 meters apart in Science Mode and 200 m apart in Standby Mode as shown in Figure 1a. The mode of interest is Science Mode where the deputy spacecraft performs maneuvers to keep the distance between the two CubeSats at 40 m, the telescope's focal length. When in Science Mode, crosslink is on continuously to monitor the satellites due to the high number of maneuvers. This makes sure the state of each satellite is consistently known from GNSS measurements [1].

When it is time to take photos for during the 10-second photo period, the spacecraft will simply drift to its position. Thrust and slew maneuvers cannot happen during this time because the motion would cause the telescope to lose focus. Upon completion of the photo period, the deputy spacecraft maneuvers to maintain a relative orbit. The system can attempt the 10-second photo period at the same orbital position in each orbit. It is of significant note that not every photo would be clear due to process noise [1].

Science Mode is the most critical part of the mission for both navigation and collisions. See Figure 2 for alignment tolerances related to the mode. In addition to these specified tolerances, it is essential that the lateral drift rate is less than 200 micrometers per second. The tolerances are tight, so monitoring possible deviations from intended orbits is essential. [1]. This mission has several critical requirements related to high-precision relative navigation, collision avoidance, omnidirectional communication, and the three degree-of-freedom propulsion system as described in the VISORS Preliminary Design Review [1]. Unaccounted orbital perturbations can significantly endanger the first two requirements and may push the satellites from their intended orbit causing mission failure. Since the exhaust plume is much denser by many orders of magnitude than the freestream at the target altitude range (500-600 km), it could be a dangerous drag source and must be taken into account very thoughtfully.

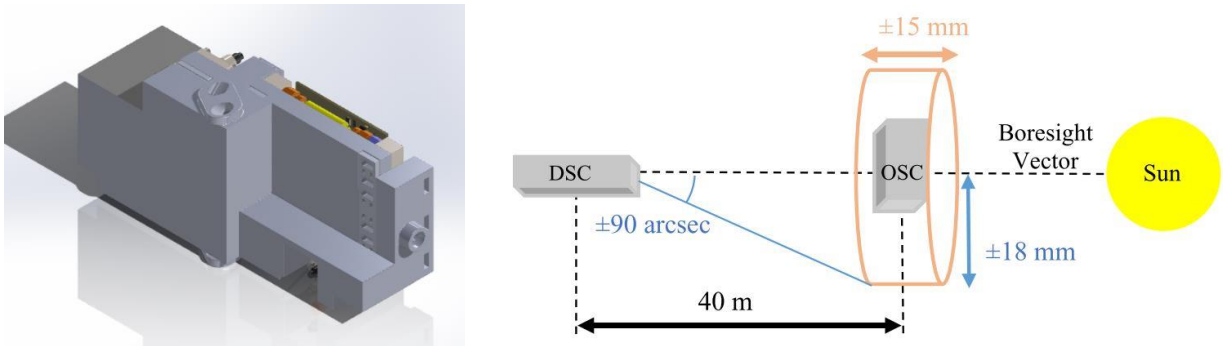

Figure 2: a) DSC Propulsion System Block; b) VISORS Orbit Tolerances [1]

1.1 Research Goals

The main goal is to analyze the leading spacecraft's (DSC) plume's effects on the trailing spacecraft (OSC). The analysis method of choice for the plume would be DSMC due to the rarefied environment which it expels into. Two plume inputs will be analyzed in this environment: 1. uniform input based on isentropic relations and 2. non-uniform input based on a CFD simulation of the flow inside the nozzle. The results will then be compared to plume models from literature in preparation to form a correlation for this particular nozzle.

1.2 Thesis Structure

Section 2 addresses the flow regimes which are segmented by the Knudsen Number. Section 3 defines what gas kinetic theory is and discusses the Boltzmann Equation and its assumptions. Section 4 discusses DSMC as well as the intermolecular interaction models, collision frequency models, energy-exchange model, and numerical accuracy of the method. Section 5 discusses analytical plume models of a circular plume issuing into a vacuum. Section 6 addresses the creation of an equivalent particle in SPARTA for HFC which cannot be modeled historically in SPARTA due to the large number of vibrational modes. Section 7 discusses CFD the selected Fluent settings chosen for the simulation of flow through the nozzle. Lastly, section 8 details the setup of the simulations which includes discussion about boundary condition calculations and the domain. Conclusions as well as future work will be discussed in Section 9.

2. FLOW REGIMES

The parameter that characterizes gas rarefaction is the Knudsen number (Kn) which is defined by Equation 1. The Knudsen number is the mean free path, λ (defined by Equation 2), divided by the characteristic length of a system, L. In Equation 2, n_{rho} is the number density or number of particles per cubic volume and d_{avg} is the average particle diameter.

$$Kn = \frac{\lambda}{L} \quad (1)$$

$$\lambda = \frac{1}{\sqrt{2} n_{nrho} * \pi * d_{avg}^2} \quad (2)$$

Flows are in the continuum regime for Kn<10^-3. Macroscopic parameters are considered, and the particles act as a unit in this regime. The flow is governed by the Navier-Stokes equations. For a gas with a Knudsen number from 10^-3 to 10^-1, the usage of the Navier-Stokes equations can be extended through slip and thermal jump boundary conditions [15].

For 10^-1 to Kn→ ∞, the flow is in the free molecular range. The gas is made up of molecules that do not behave as a continuous fluid in the free molecular range. The collisions are mostly gas-surface collisions in these free molecular systems, with the rarefied gas behaving on a particle-on-particle basis with little or no interaction between the particles. Here the flow is governed by the Collisionless Boltzmann Equation [15].

Between these two regimes for 10^-1<Kn<10^1, the transitional regime where both intermolecular and gas-surface collisions must be considered. Here the flow is governed by the Boltzmann Equation (with collisions) as the Navier-Stokes equations cannot describe the non-equilibrium and viscous effects [15].

The plume simulation for the VISORS system is within in the free molecular regime governed by the Boltzmann Equation, solved via DSMC. The atmosphere is thin at 500-650 km, and the reference length is also relatively small for a CubeSat putting the Knudsen number within this particular range. For analysis of the nozzle, it is assumed that the gas flow regime is continuum inside the nozzle and can be resolved using CFD. Figure 3 represents the Knudsen number range and corresponding flow regimes [15].

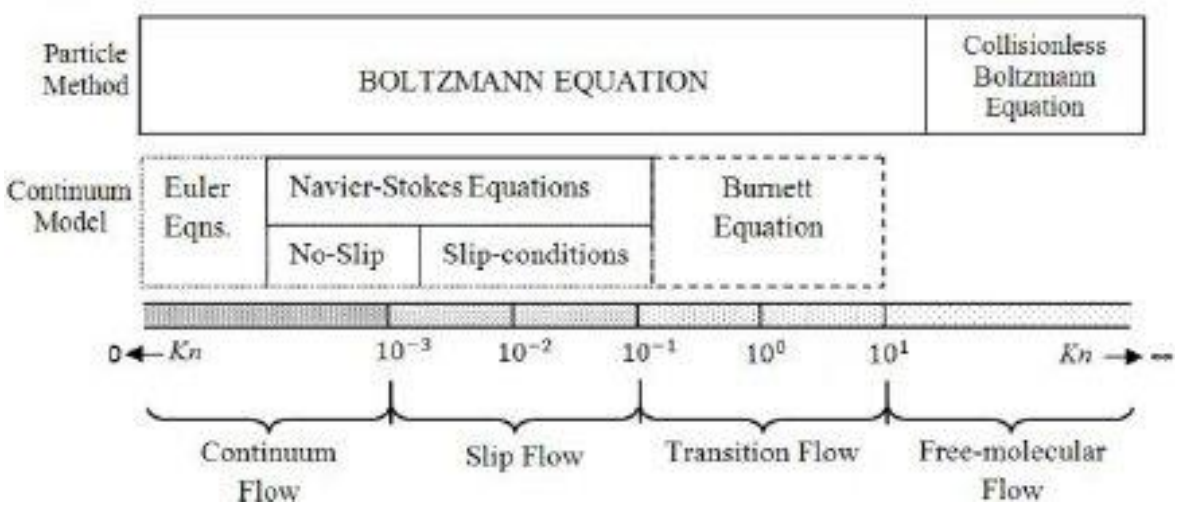

Figure 3. Knudsen numbers and model applicability [15]

3. GAS KINETIC THEORY

The gas kinetic theory considers microscopic properties (motion, molecular energy transfer, and molecular composition) to explain macroscopic, observable properties (temperature, pressure, and bulk flow velocity). The gas kinetic theory has four postulates. The first postulate is a *molecular hypothesis* that says that the gas molecules are in constant, random motion. A unit molecule of a pure chemical substance keeps both its chemical properties and composition. The second postulate is *ideal gas* which says molecules only exert forces on each other during collisions. The third postulate is *dilute gas* where only binary collisions are probable because the average distance separating particles is large when compared to the size of the particles. Lastly, the classical mechanics postulate states that quantum-mechanical and relativistic effects are negligible. Gas kinetic theory is statistical as it is impossible to model every particle. Probabilities of finding a molecule in a particular position and state is used. One can then gather macroscopic properties by averaging molecular values over a small volume. [16]

3.1 Boltzmann Equation

The Boltzmann Equation is the governing equation which is used for rarefied gas dynamics. The assumptions used to obtain it include :

1. There are only binary collisions,

2. Molecular Chaos (assumes there is an infinitely large number of particles in the system)

3. The distribution function has no changes over distances on the order of a molecule's diameter [16] .

The Boltzmann equation (Equation 3) only has one variable, f or the velocity distribution function. It is a function of t (time), $\vec{X}$ $(position)$, and $\vec{C}$ $(velocity)$. The variable describes the probability of finding a particle in a particular position with a particular speed [16], [17] . Other variables in the equation are $\vec{F}$ $(external\ force)$, $[g, b, \epsilon](collision\ parameters)$, n_{rho} $(number\ density)$, m (mass), and $\vec{Z}$ $(velocity\ of\ other\ collisional\ partner)$.

$$\frac{\partial(n_{rho}f)}{\partial t} + \overrightarrow{C}.\nabla_X(n_{rho}f) + \frac{\vec{F}}{m}.\nabla_C(n_{rho}f) = \int n_{rho}^2(f'f_z' - ff_z)gbdbd\epsilon d\vec{Z} \qquad (3)$$

4. DSMC SIMULATIONS

The Direct Simulation Monte Carlo (DSMC) method is used to analyze rarefied systems numerically. G.A. Bird proposed DSMC in the 1960s specifically to model rarefied gas dynamics [18]. This method is not an explicit solution, but it is based on molecular free-flight and collisions, the processes which the Boltzmann Equation considers [17]. It is a probabilistic technique that models a certain number of real particles using a simulated particle and integrates the system positions in time using particle velocities. It uses statistical chemistry, physics, and the kinetic theory of gases.

This method allows the flow to be analyzed on a particle-on-particle basis. The DSMC algorithm can be seen in Figure 4 [16]. Both time and space are discretized for this algorithm. The DSMC code of choice is SPARTA, an open-source code from Sandia Labs [36]. The DSMC algorithm consists of two major steps. There is a "move" step and a "collide" step. The molecular interactions are binary, and the collision scheme generally chooses the frequency of collisions [18].

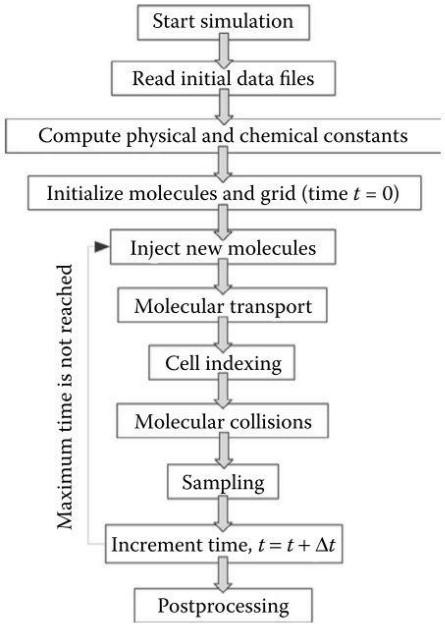

Figure 4. DSMC Algorithm Flowchart [16]

4.1 Intermolecular Interactions Overview

The binary interactions between molecules in DSMC simulations can be modeled in various ways. In SPARTA, the interaction models are applied via a two-step algorithm. The total collision cross-section, σ_T, is used to calculate both collision pairs and collision frequency. Next, a particular scattering law is used. Scattering laws describe post-collisional velocities using pre-collisional velocities and trajectories. The outcome of such a collision can be entirely described by the deflection angle, χ, which is the angle between pre-collisional and post-collisional velocities [18].

Only two impact parameters and the translational velocities of the molecules are needed to describe the binary elastic collision for spherically symmetric molecules. The parameters are b (the distance of closest, undisturbed approach in the center of mass reference frame) and ϵ (the angle between the collision plane and reference frame) [18]. The total cross section is given by Equation 4 [16]–[18] while Figure 5 shows the collision geometry of the system [17].

$$\sigma_T = 2\pi \int_0^{\pi} (\sigma \sin\chi) d\chi \quad where \quad \sigma = \left(\frac{b}{sin\chi}\right) \left|\frac{db}{d\chi}\right| \tag{4}$$

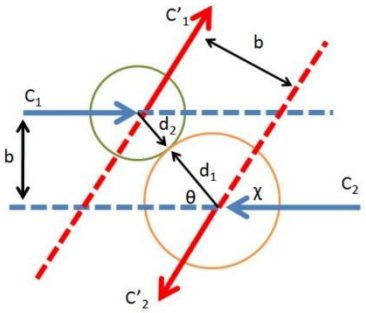

Figure 5: Collision Geometry [17]

4.2 Collision Dynamics

The intermolecular force given between two molecules is F and the intermolecular potential is Φ. The molecular model is established by the definition of either of these parameters which are related through Equations 5 and 6 [18].

$$\theta = \int_r^{\infty} F\, dr \tag{5}$$

$$F = -\frac{d\Phi}{dr} \tag{6}$$

The equation of orbit produced based off intermolecular potential is given by Equation 7 [18] which relates position (r, θ), the distance of undisturbed approach (b), the relative molecular speed (c_r), and the reduced mass ($m_{reduced} = \frac{m_1 m_2}{m_1 + m_2}$) [8].

$$\left(\frac{dr}{d\theta}\right)^2 = \frac{r^4}{b^2} - r^2 - \frac{\Phi r^4}{\frac{1}{2} m_{reduced} c_r} \quad (7)$$

4.2.1 Hard Sphere Molecular Model

Because the hard sphere (HS) model describes the molecules as rigid spheres, Equations 8 and 9 can be derived for the total collision cross section and the deflection angle [18]. Note that the molecule diameter used is just the average of the diameters for the collision pair.

$$\sigma_{T_{HS}} = \pi d_{12}^2 \quad where\ d_{12} = \frac{d_1 + d_2}{2} \quad (8)$$

$$\chi_{HS} = 2cos^{-1}\left(\frac{b}{d_{12}}\right) \quad (9)$$

Because the total collision cross section is independent of deflection angle, the scattering of the molecules for this model are isotropic. This means all directions are equally likely for the post-collisional relative speed, c_r^* [18].

4.2.2 Variable Hard Sphere Molecular Model

Bird proposed the Variable Hard Sphere (VHS) model in 1981 [18]. It follows the hard sphere model but substitutes the average molecule diameter as an Inverse Power Law (IPL) function of relative collision energy between molecules. The diameter used for Variable Hard Sphere to find the deflection angle and total collision cross section is defined in Equation 10. [16]–[18].

$$d_{VHS} = d_{ref}\left(\frac{c_{r,ref}}{c_r}\right)^{\nu} \quad (10)$$

In this equation, d_{ref} is the reference diameter, c_r is the relative molecular speed, $c_{r,ref}$ is a reference relative molecular speed and ν is the power law exponent.

4.2.3 Variable Soft Sphere Intermolecular Model

The variable soft sphere (VSS) model follows the variable hard sphere (VHS) model for the total collision cross section which is calculated from the inverse power law function diameter. The only difference between these two models is that the deflection angle equation takes into consideration the scattering parameter, α, which lies between a value of 1.0 (completely specular, mirrored reflection) to 2.0 (completely diffuse). Equation 11 is the deflection angle for the (VSS) model [18]. Specular and diffuse reflections can be seen in Figures 6 and 7 [17].

$$\chi_{VSS} = 2\cos^{-1}\left(\frac{b}{d_{VSS}}\right)^{\frac{1}{\alpha}} \quad where\ d_{VSS} = d_{VHS} \tag{11}$$

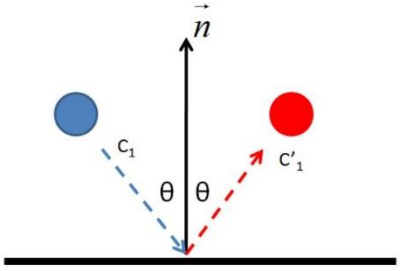

Figure 6: Specular Reflection [17]

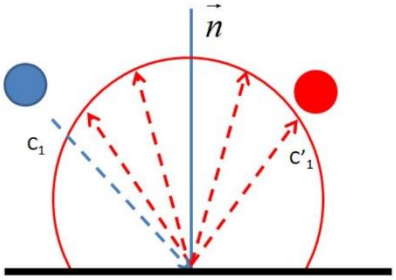

Figure 7: Diffuse Reflection [17]

4.3 No-Time Counter Collision Frequency Model

G.A. Bird introduced the No-Time counter scheme in 1989 [18]. N_{coll}, the number of potential collision pairs is below. F_{NUM} is the number of real particles per cell over the number of simulated particles per cell. σ_T is the total collision cross-section , c_r is the relative velocity, Δt

is the change in time, ΔV is the volume change, and N is the number of particles. Equation 12 details the scheme.

$$N_{coll} = \frac{1}{2} * \frac{N(N-1)F_{NUM} * max(\sigma_T c_r)\Delta t}{\Delta V} \quad (12)$$

The system chooses $Ncoll$ random pairs and accepts a collision for the probability, $\frac{\sigma_T c_r}{\max(\sigma_T c_r)}$ [19].

4.4 Majorant Collision Frequency Model

The majorant frequency is computed by the Majorant Collision Frequency scheme to find the local timestep, δt. Equations 13 and 14 detail the scheme with the same symbols as defined by the No Time-Counter Scheme.

$$\max(\nu) = \frac{1}{2} * \frac{N(N-1)F_{NUM} * max(\sigma_T c_r)}{\Delta V} \quad (13)$$

$$\delta t = -\frac{lnR}{\max(\nu)} \quad (14)$$

The only new variable here is R, a random number uniformly distributed between 0 and 1. The collision pairs are chosen at random. The probability for accepted collisions is, $\frac{\sigma_T c_r}{\max(\sigma_T c_r)}$. The denominator of this probability can change, so the majorant frequency is computed again as well as δt . The process repeats until the following is true (Equation 15) [18], [19].

$$\sum \delta t \leq \Delta t \quad (15)$$

4.5 Internal Energy Exchange Model: Larsen-Borgnakke

The Larsen-Borgnakke (LB) model describes the energy exchange between molecules in particle collisions [16]. The two energy modes are translational and vibrational. Many internal energy exchange models can be computationally expensive. Of the those models, the LB model is the most cost-effective. The LB model assumes the rotational and vibration mode's energy spectrums to be continuous. In addition to this, post-collisional energies are taken from the Boltzmann distribution. The fraction of inelastic collisions is determined by the following values, $1/Z_r$ and $1/Z_v$. These values are the probability of a select pair of molecules having a translational-rotational energy exchange. The denominators of these values are called the

collision numbers. They also determine the number of collisions required for vibrational and rotational equilibrium. [16]

4.6 Numerical Accuracy

There are a few rules that were used for these DSMC simulations. The timestep is generally the smaller of the mean collision time (mct, Equation 16) or the mean traveling time (mtt, Equation 18) divided by 10 to ensure a sufficiently small timestep where cells are not skipped in iterations. The mean thermal velocity, c', used in Equation 16 is defined by Equation 17. Lastly, minimum number of cells in a particular direction is given by Equation 19. As for definitions of the symbols: k_b is the Boltzmann Constant, m is the mass of a single particle, T is temperature, L is the length of the domain in a particular direction, Δl is the size of a cell, m is mass, and V_{inf} is the freestream velocity.

$$mct = \frac{\lambda}{c'} \tag{16}$$

$$\bar{c}' = \sqrt{\frac{8 * k_b * T}{\pi * m}} \tag{17}$$

$$mtt = \frac{\Delta l}{V_{inf}} \tag{18}$$

$$\text{minimum number of cells in x, y, z} = \frac{L}{\frac{\lambda}{3}} \tag{19}$$

It is of note that there should be a minimum of 20 simulated particles per cell, but most simulations use hundreds per cell. The number density, n_{rho}, and F_{NUM} (number real particles per cell/number of simulated particles per cell) control this in SPARTA [20].

5. NUMERICAL PLUME MODELS

Several numerical models exist to describe the dense plume. This work explores three models: the Gerasimov, Roberts-South, and Simons-Boynton models [3]-[14]. To get a simplified cross-section of the center of the plume, the cylindrical coordinate system of these models is simplified (Z=0). Equations 20 and 21 define a 2D cross-section directly at the plume's center while Figure 8 gives a visual representation of the coordinate system.

$$r = \sqrt{X^2 + Y^2} \qquad (20)$$

$$\theta = \arctan\left(\frac{Y}{X}\right) \qquad (21)$$

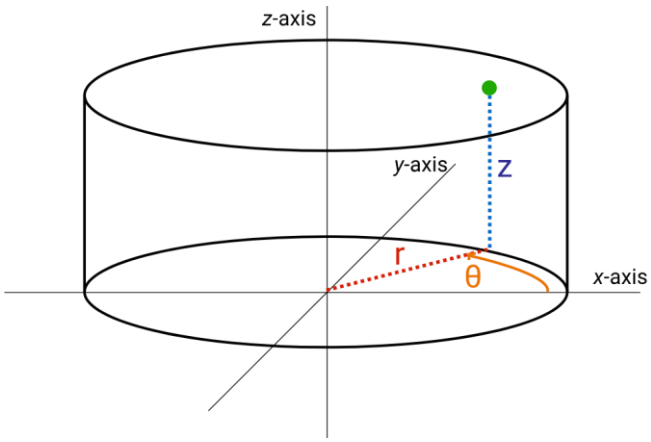

Figure 8: Cylindrical Coordinate System [21]

5.1 Gerasimov Model

The Gerasimov model (RSC "Energia") is an analytical model for plumes. It assumes a point source where intensity changes with angle and that the gas is a supersonic, ideal gas plume. The range of applicability is $\theta_+ = 15 - 33\ degrees$ ($\theta^0 approximately\ 3$), $M_e = 1 - 5$, $\gamma = 1.2 - 1.4$, and $\frac{r}{r_e} > 10$. The following equations and definitions describe the model (Eq 22-27) [12]-[14].

$$\rho(\theta) = \rho(0) exp\left[-0.5\left(\frac{\theta}{\theta_+}\right)^2\right] \qquad (22)$$

$$\rho(0) = \frac{\rho_e A(\gamma-1)^{0.5}}{\left[\left(\frac{r}{r_e}\right)^2 F\,\theta_+^2\right]} \qquad (23)$$

$$\theta_+ = arctg\sqrt{\frac{(1-I)}{I}} \quad (24)$$

$$A = 8^{-0.5}\left[\frac{2}{\gamma+1}\right]^{(\gamma+1)/[2(\gamma-1)]} \quad (25)$$

$$I = \left(1+\frac{1}{\gamma M_e^2}\right)\left[1+\frac{2}{(\gamma-1)M_e^2}\right]^{-0.5} \quad (26)$$

$$F = \left(\frac{R_e}{R^*}\right)^2 \quad (27)$$

Variables

- $\rho = density$
- $R = nozzle\ radius$
- $r = radial\ position,\ \sqrt{x^2+y^2}$
- $\theta = angular\ position,\ tan^{-1}\left(\frac{y}{x}\right)$
- $M = Mach\ Number$
- $\gamma = ratio\ of\ specific\ heats$

Subscripts

- $e = nozzle\ exit$
- $0 = stagnation$
- $* = sonic\ throat$

5.2 Boynton-Simons Model

The Boynton-Simons Model is an analytical density solution based on expanding a nozzle boundary layer into a vacuum. It assumes point source, that exit conditions are taken only from the viscous layer, and inviscid expansion. It also states that Boynton's choice for f(θ) was chosen by constraining it to obey locally 2D Prandtl-Meyer functions for theta near limiting turning angle and by considering correlations of numerical results. Because of the point source assumption, the flow is not accurate close to the nozzle. It has also been shown that the density in the plume at large angles from the centerline is a sensitive function of the ratio of the nozzle boundary layer thickness to the exit radius. The following equations and definitions describe the model (Eq 28-33) [3]-[8].

$$\frac{\rho}{\rho^*} = A\left(\frac{R^*}{r}\right)^2 f(\theta) \quad (28)$$

$$f(\theta) = \cos^{\frac{2}{\gamma-1}}\left[\left(\frac{\pi}{2}\right)\left(\frac{\theta}{\theta_\infty}\right)\right] \quad (29)$$

$$A = \frac{\frac{U^*}{2U_l}}{\int_0^{\theta l} f(\theta)\sin(\theta)d\theta} \quad (30)$$

$$U_l = \left(\frac{\gamma+1}{\gamma-1}\right)^{\frac{1}{2}} \mathrm{U}^* \quad (31)$$

$$\theta_l = \frac{\pi}{2}\left(\sqrt{\frac{\gamma+1}{\gamma-1}} - 1\right) \quad (32)$$

$$\theta_\infty = \theta_l \; for \; invicid \; supersonic \; flow \quad (33)$$

Variables

- $\rho = density$
- $R = nozzle\ radius$
- $r = radial\ position,\ \sqrt{x^2 + y^2}$
- $\theta = angular\ position,\ tan^{-1}\left(\frac{y}{x}\right)$
- $U = velocity$
- $\gamma = ratio\ of\ specific\ heats$

Subscripts

- $* = sonic\ throat$
- $l =$ limiting
- $\infty =$ inviscid supersonic flow

5.3 Roberts and South Model

The Roberts and South Model is an analytical density solution for a plume based on mass and momentum flux in the jet. Its assumptions include: that the density profile of $\cos^k(\theta)$ is assumed where $k = \gamma(\gamma - 1)M_e^2$ and also that when the flow leaves the exit as isentropic. It is of note to say that the model is not accurate in the near-field due to the singularity in the denominator near the exit at r=0. Additionally, the solution is sensitive to large angles. The following equations and definitions describe the model (Eq. 34-37) [9]-[11].

$$\frac{\rho}{\rho_e} = \frac{k}{2}\left(\frac{R_e}{r}\right)^2 \cos\left(\frac{\theta}{\theta_\infty}\right)^k \quad (34)$$

$$k = \gamma(\gamma - 1)M_e^2 \quad (35)$$

$$\theta_l = \frac{\pi}{2}\left(\sqrt{\frac{\gamma+1}{\gamma-1}} - 1\right) \quad (36)$$

$$\theta_\infty = \theta_l \text{ for invicid supersonic flow} \quad (37)$$

Variables

- $\rho = density$
- $R = nozzle\ radius$

- $r = radial\ position,\ \sqrt{x^2 + y^2}$
- $\theta = angular\ position,\ tan^{-1}\left(\frac{y}{x}\right)$
- $M = Mach\ Number$
- $\gamma = ratio\ of\ specific\ heats$

Subscripts

- $e = nozzle\ exit$
- $l = limiting$
- $\infty = inviscid\ supersonic\ flow$

6. HFC THEORETICAL PARTICLE

The refrigerant used in this mission is HFC-236fa, a non-linear polyatomic molecule. Because of its large number of vibrational modes, it is necessary to create an equivalent, "artificial" particle specifically for SPARTA. A particle has been created that matches closely in both viscosity and Cp (specific heat, constant pressure). The actual HFC parameters can be seen in Table 1. Additionally, NIST data for DOF(vib) is also shown in Figure 9, exemplifying the need to create an equivalent species.

Table 1: Actual Propellant Information [22]

Chemical Formula	C3H2F6
MW (amu)	152
Mass (kg)	2.525×10^{-25}
Rotational DOF	3
# of Vibrational Modes	27

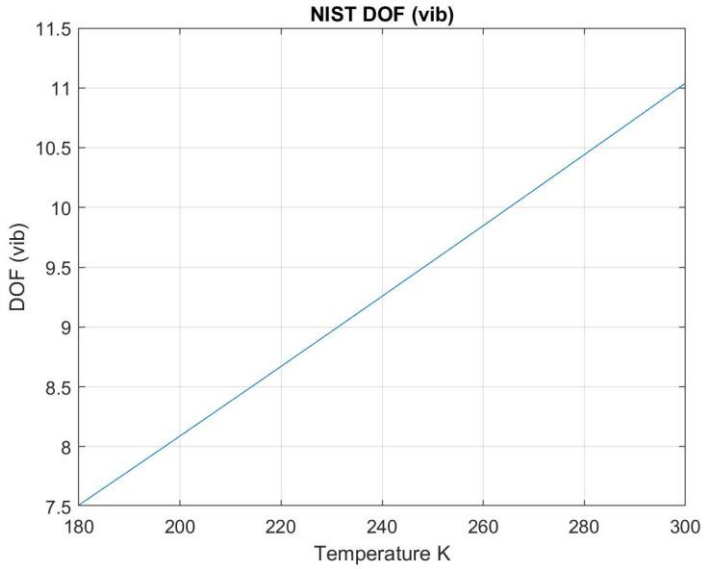

Figure 9: DOF(vib) vs T from NIST Data [23]

First, a fit is done of the following Equation 38 [18] where omega is chosen to be of the range, 0.50<=omega<1. In terms of the viscosity, data was extracted from literature [27] for use in Equation 38.

$$\mu = \mu_{ref}\left(\frac{T}{T_{ref}}\right)^{\omega} \tag{38}$$

Second, following the fit of Equation 38, the particle diameter was then calculated using the calculated omega using Equation 39 [18]. Reference parameters were extracted again from literature [27].

$$d_{ref} = \left(\frac{15}{8}\sqrt{\frac{mkT_{ref}}{\pi}}\frac{\Gamma(2.5-\omega)}{\mu_{\mathrm{ref}}\Gamma(4.5-\omega)}\right)^{\frac{1}{2}} \tag{39}$$

Third, DOF (vib) is calculated using one mode and a chosen characteristic vibrational temperature for pseudo species. Using values from a previous IQmol calculation performed by a colleague, the respective DOF(vib) was calculated for 27 modes for comparison using the following Equation 40 and values from the simulation seen in Table 2: Representative IQmol Calculation Values for HFC [2],[24].

Table 2: Representative IQmol Calculation Values for HFC [2],[24]

Modes	**Characteristic Vibrational Temperature, Θ (K)**
1	40.7
2	176.4
3	237.4
4	463.2
5	469.2
6	513.6

$$\mathrm{DOF}_{\mathrm{vib}} \sum_{\mathrm{i}=1}^{\mathrm{n}} \frac{\left(\frac{\theta_{\mathrm{i}}}{\mathrm{T}}\right)^{2} \mathrm{e}^{\frac{\theta_{\mathrm{i}}}{\mathrm{T}}}}{\left(\mathrm{e}^{\frac{\theta_{\mathrm{i}}}{\mathrm{T}}}-1\right)^{2}} \tag{40}$$

Fourth, the equipartition law of energy can be used to derive a relation between DOF(vib) and Cp for HFC-fa236. It states that in thermal equilibrium energy is shared equally between all degrees of freedom: translational, rotational, vibrational, and electronic. This means the average kinetic energy of one form per DOF (Degrees of Freedom) to be equal to the average kinetic energy of another form per DOF. With the equipartition law of energy, the following derivation for a relation between DOF(vib) and Cp was derived for HFC-fa236. e is internal energy, R is the specific gas constant, T is temperature, and Cv and Cp are the specific heats (constant volume and pressure respectively). The average kinetic energy per DOF is equal to 1/2RT or in the specific case of vibrational energy where two molecules are necessary, RT. Notably, there are both 3 rotational and 3 translational DOF for HFC. The derivation is listed in lines numbered 1 through 8 [22],[34].

1. $e = e_{tran} + e_{rot} + e_{vib}$
2. $e = \frac{3}{2}RT + \frac{3}{2}RT + DOF_{vib}RT$
3. $\frac{de}{dT} = \frac{3}{2}R + \frac{3}{2}R + DOF_{vib}R$
4. $Note: Cv \equiv \frac{de}{dT}$
5. $\frac{Cv}{R} = 3 + DOF_{vib}$
6. $Note: \frac{Cp}{R} = \frac{Cv}{R} + 1$
7. $\frac{Cp}{R} - 1 = 3 + DOF_{vib}$
8. $\boldsymbol{DOF_{vib} = \frac{Cp}{R} - 4}$

The gas constant is calculated from a chosen MW, a chosen characteristic vibrational temperature, and a chosen DOF(vib)=1. All are plugged into the equation (line 8) that was derived for DOF(vib) as a function of Cp in order to fit the Cp values to match as close as possible to the NIST Cp variation [26] with temperature. Once an adequate MW and characteristic temperature are chosen, particle mass can be calculated [2].

Finally, the rotational DOF is chosen as the max in SPARTA and alpha is chosen from VSS as 1.6 (a value from 1.0 to 2.0). The rest of the values in the VSS parameter file as well as the species file for SPARTA are the same as they are for N2 [2]. Figures 10 and 11 can be produced

from this process by comparing actual HFC to the artificial HFC particle. The final values for the SPARTA files are listed in Table 3.

Table 3: Equivalent HFC Parameters [2],[24]

MW	52 kg/kmol
mass	8.8E-26 kg
d_{ref}	7.0994E-10 m
ω	.999
DOF_{rot}	2
α **(VSS)**	1.6
Θ (N = 1 mode)	791
DOF_{vib} **(N=DOF/2)**	2

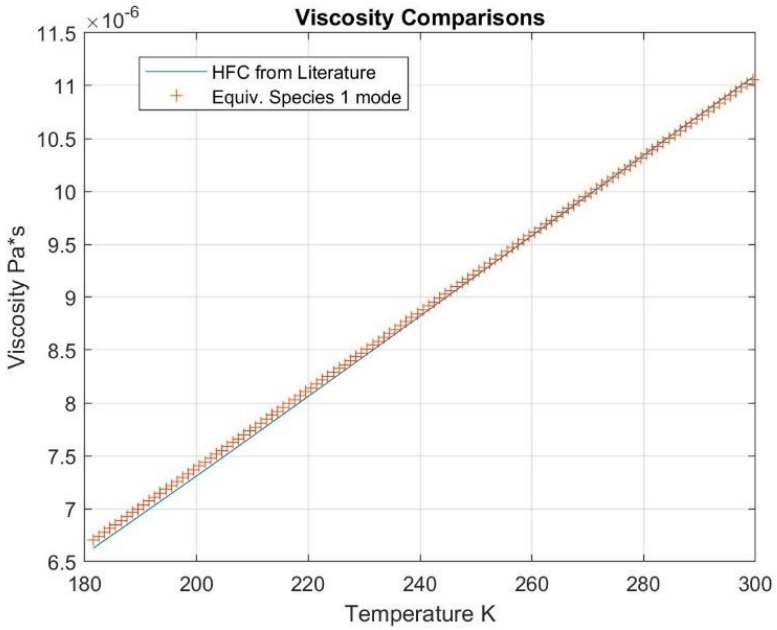

Figure 10: Viscosity Comparisons between HFC from Lit. and the Equiv. Species [27]

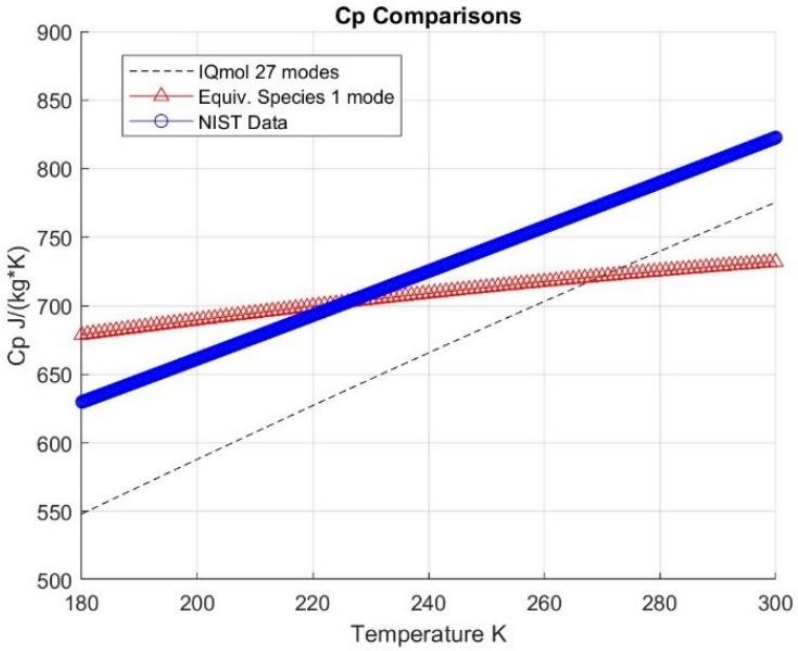

Figure 11: Cp Comparisons between HFC with 27 modes, the Equiv. Species IQmol [2],[23]; Equiv Species [24],[25]; NIST [26]

7. CFD SIMULATIONS METHODOLOGY

Computational Fluid Dynamics (CFD) is defined as "a branch of fluid mechanics that uses computer based numerical analysis and algorithms to simulate, analyze and solve problems in fluid flow" [37]. The equations solved in CFD simulations are the Navier-Stokes equations. The conservation equations for mass and momentum are solved and an additional equation for energy conservation is solved if the flow is compressible [35].

While boundary conditions used for the CFD simulations will be described under section 8, the basic settings used in Fluent (a CFD software), will be detailed here. The CFD simulation is simulating a nozzle flow to acquire a non-uniform input. The flow is assumed to be continuum from the nozzle throat to exit. The solver used was density-based, velocity formulation was chosen to be absolute, the problem is steady, and it is also 2D axisymmetric. The energy model was used and the flow is assumed to be laminar for the initial run. To check this assumption k-omega SST was used in comparison to the laminar model. This assumption stems from the idea that the flow does not have time to fully develop. When the external Re was calculated at both the inlet and exit, they fell well below the turbulent limit. Methods used include implicit, AUSM, Least Squares Cell Based, Second Order Upwind, and High Order Term Relaxation. The initialization was standard, computed at the inlet and relative to the cell zone [35].

As for defining HFC in fluent, density was calculated from ideal gas while Cp (the specific heat at constant pressure), thermal conductivity, and viscosity are from kinetic theory. The molecular weight of actual HFC is used, 152.04 kg/kmol while the L-J Characteristic Length = 5.644 Angstrom and L-J Energy Parameter = 307.24 K are pulled from a report [29]. The DOF of HFC is equal to 42 where N=8 in the following equation where DOF=6N-6 for non-linear molecules [29]. Figure 12 is an image of the HFC molecule.

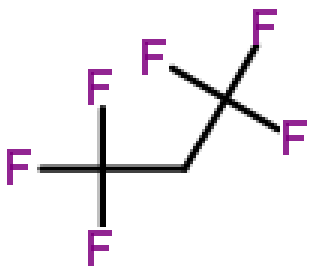

Figure 12: HFC Molecule [30]

8. SIMULATIONS AND RESULTS

The details of the CFD and DSMC simulations, including boundary conditions specification, domain setups, and mesh sizes, are presented in this section. Because plume impingement is critical to the success of the mission, the main goal of these simulations is to compare a DSMC simulated plume to plumes calculated by analytical models in order to gain insight into the plume's behavior. As stated earlier, this information will be used to form a correlation for the nozzle and operating conditions to save on computational time for future plume impingement studies.

The first simulation is of the VISORS nozzle in Fluent expelling into a adiabatic, inviscid duct. The goal is to acquire the non-uniform conditions at the exit of the nozzle which considers the effect of the walls of the nozzle. This input will be used later to analyze the extent of the nozzle walls' influence by comparing the non-uniform CFD-based input to the uniform isentropic-based input to see how much of a difference the wall effects make on the flow. This simulation was done in Fluent using CFD assuming that the flow is continuum and laminar from the nozzle throat to exit.

The second simulation and third simulations were performed using DSMC. The main idea of these simulations was to simulate the non-uniform and uniform inputs each expelling into a vacuum in SPARTA. The goal is to compare the plumes resulting from these inputs to several analytical plume models from literature. This would give more insight as to which model to start from in order to form a correlation for the VISORS nozzle for future use. The freestream was neglected here.

The given nozzle parameters include [31]:

- $M_{throat} = 1$
- $T_o = 298$ K
- $R_{throat} = .35E-3m$
- $R_{exit} = 5E-3\ m$
- $Isp = 43\ s$
- $Thrust = 40E-3\ N$

- $\gamma = 1.083$
- $MW_{HFC} = 152.04 \frac{g}{mol}$
- $Altitude = 500E3$
  $(need\ this\ for\ MSIS90\ atmospheric\ data\ and\ calculation\ of\ g_o)$

The values at the throat of the nozzle were calculated for CFD by the following method:

1. $T_{throat} = T_o \left(1 + \frac{\gamma-1}{2} M_{throat}^2\right)^{-1} = 286.1258\ K$ (Isentropic)
2. $V_{throat} = M_{throat} * \sqrt{\gamma R T_{throat}} = 130.1724 \frac{m}{s}$ (Mach definition)
3. $mdot = \frac{Thrust}{Isp\ g_o}$ (Thrust-Isp Relation)
4. $rho_{throat} = \frac{mdot}{V_{throat} A_{throat}}$ (Continuity)
5. $p_{throat} = rho_{throat} R\ T_{throat} = 34462.7933\ Pa$ (ideal gas)

The values at the atmospheric pressure outlet were calculated for CFD by the following method:

1. $\rho_{ext} = 2.7765E-13 \frac{kg}{m^3}$ $(MSIS90)$ [32]
2. $nrho_{ext} = 4.99E12 \frac{1}{m^3}$
3. $T_{ext} = 713.6\ K$
4. $T_{o_{ext}} = 298\ K\ (extrapolated)$
5. $p_{ext} = nrho_{ext} k_b T_{ext} = 4.9140E-8\ Pa$

Lastly, the uniform plume input calculation for DSMC, SPARTA, is detailed below:

1. $\frac{A_{exit}}{A_{throat}} = \frac{\gamma+1}{2}^{-\frac{(\gamma+1)}{2(\gamma-1)}} \frac{\left(1+\frac{\gamma-1}{2} M_{exit}^2\right)^{\frac{\gamma+1}{2(\gamma-1)}}}{M_{exit}}$
2. $T_{exit} = T_o \left(1 + \frac{\gamma-1}{2} M_{exit}^2\right)^{-1} = 166.5363\ K$ (Isentropic)
3. $V_{exit} = M_{exit} * \sqrt{\gamma R T_{exit}} = 433.1309 \frac{m}{s}$ (Mach definition)
4. $mdot = \frac{Thrust}{Isp\ g_o}$ (Thrust-Isp Relation)
5. $rho_{exit} = \frac{mdot}{V_{exit} A_{exit}}$ (Continuity)

6. $p_{exit} = rho_{exit} R\, T_{exit}$ (ideal gas)
7. $nrho_{exit} = \frac{p_{exit}}{k_b T_{exit}} = 1.2853E22 \frac{1}{m^3}$

The CFD domain is shown in Figure 13 with pure HFC issuing from the Velocity-Inlet and exiting out into an inviscid- adiabatic duct. The simulation is axisymmetric.

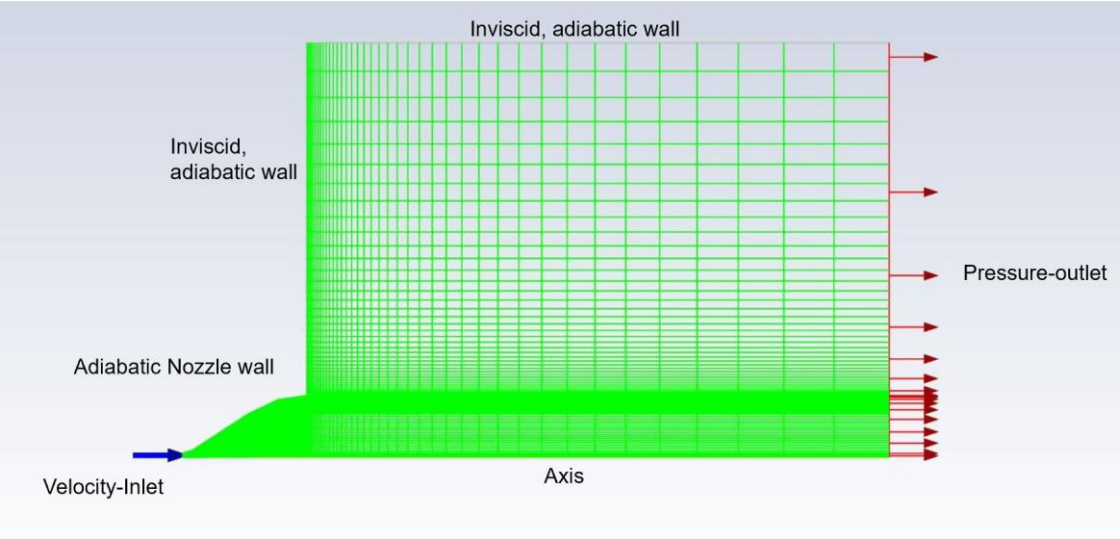

Figure 13: CFD Domain, Boundary Conditions and Computational Mesh

The DSMC domain is shown below in Figure 14 with Pure HFC issuing into a vacuum with an F_{NUM}=1E16 and a of timestep=1e-8 sec:

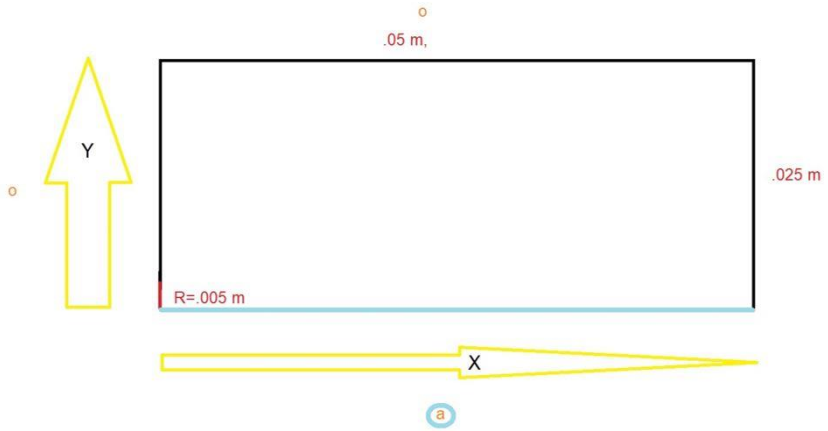

Figure 14: DSMC Domain with Boundary Conditions

The coarse CFD mesh had 13,840 cells while the medium and fine CFD meshes had 69,200 cells 290,640 cells respectively. All meshes are structured and were built using a blocking method in ICEM Mesher. [33] The mesh sizes for DSMC are: 150x75, 200x115, and 250x150 for coarse, medium, and fine meshes, respectively.

8.1 CFD: Laminar Assumption and Continuum Assumption Checks

From a turbulent CFD test case using the coarse mesh, turbulent kinetic energy (TKE) was plotted to see the levels in order to check the assumption that the flow is laminar. If the TKE levels are close to zero, then that means the flow is likely laminar. See Figure 15. TKE indicates minor turbulence which can be overlooked if the exit conditions converge between the laminar and turbulent runs.

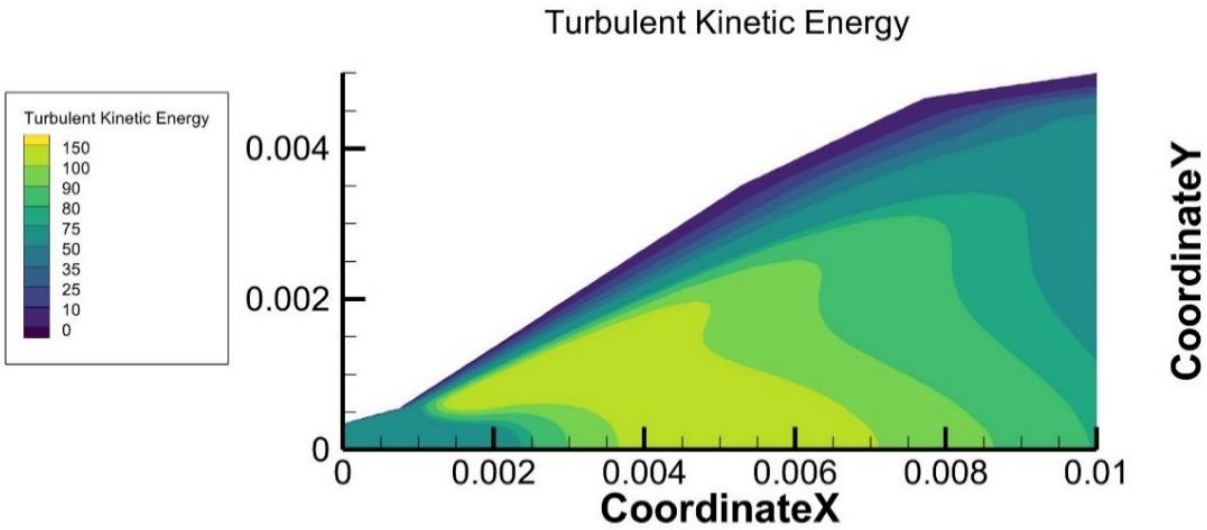

Figure 15: TKE in Nozzle, k-omega SST

Since the TKE levels have a wide range, not just close to zero, the laminar test case nozzle exit plane values were then compared to the turbulent results using the same coarse mesh to see how much they differ. See Figure 16, 17, and Figure 18. All plots show adequate convergence to the same solution. This means the flow is very close to laminar despite having TKE values near 100 in certain regions. The assumption of laminar holds up.

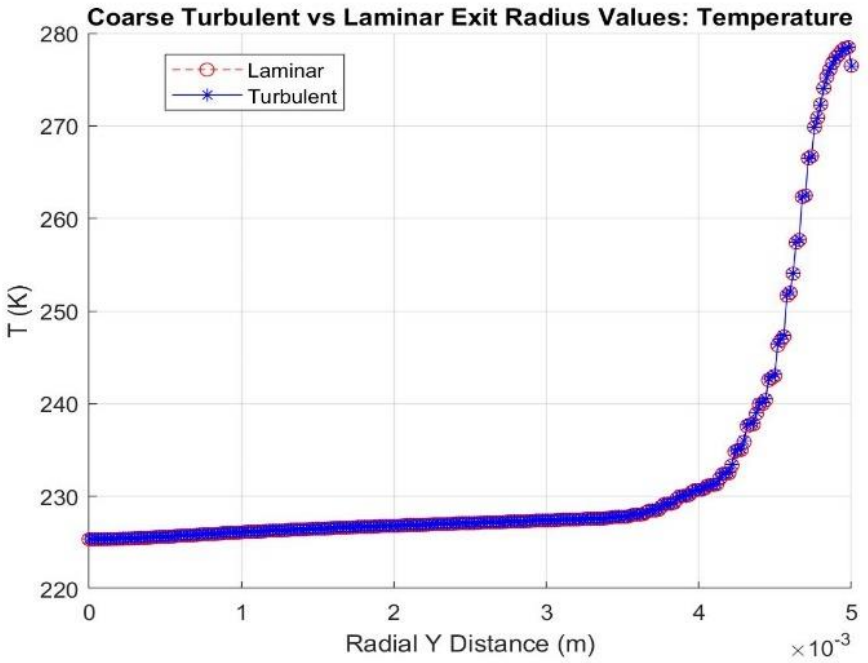

Figure 16: Exit Radius Values, Turbulent vs Laminar, Temperature

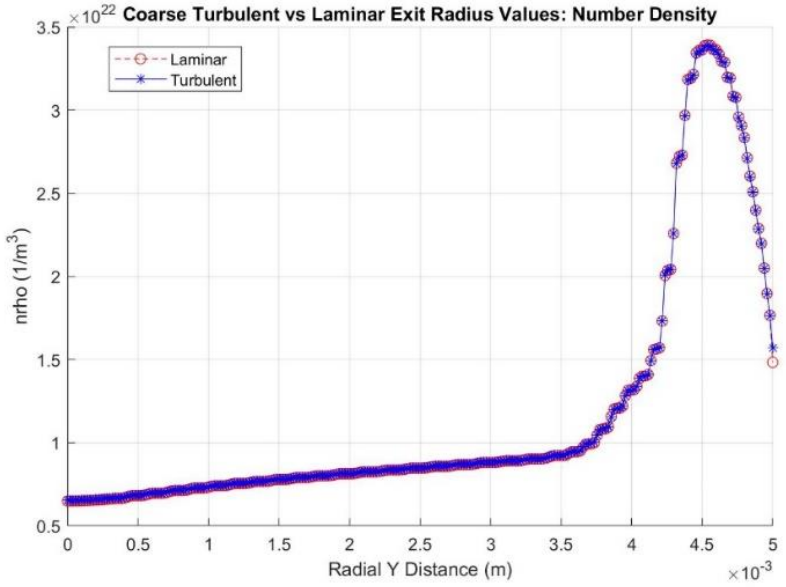

Figure 17: Exit Radius Values, Turbulent vs Laminar, Number Density

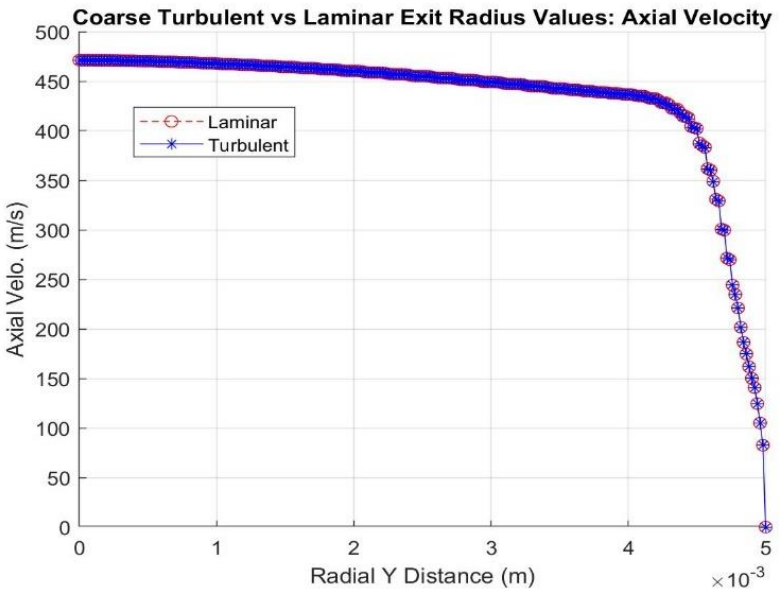

Figure 18: Exit Radius Values, Turbulent vs Laminar, Axial Velocity

The assumption in which the flow is continuum inside the nozzle was checked. The Knudsen number (Kn) was plotted at the exit of the nozzle to see the levels (Figure 19).

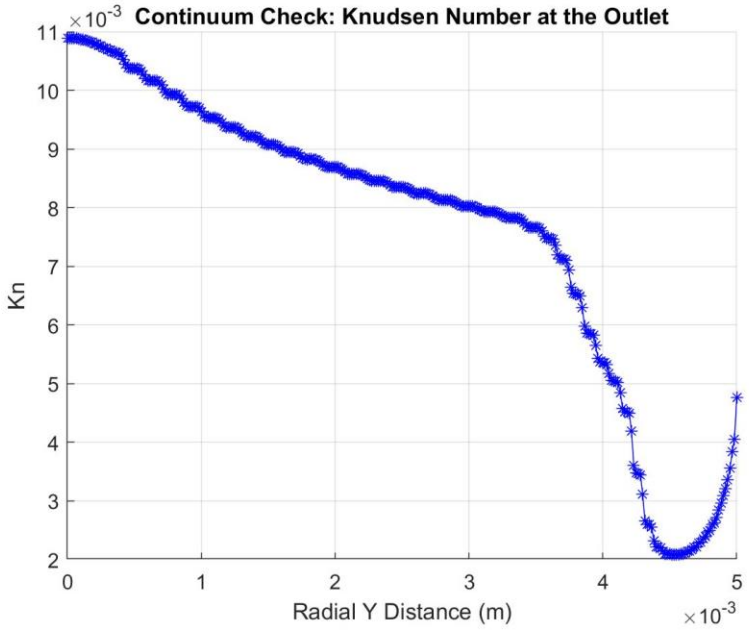

Figure 19: Exit Radius Values: Kn\

Kn < ~1E-3 which means the flow is in the continuum-slip regime. Slip flows are able to be modeled in Fluent. Therefore, the assumption that the flow is continuum and that CFD can be used holds up [15].

8.2 CFD: Laminar Results and Grid Sensitivity Study

The grid sensitivity study for the laminar run is shown in Figure 20 and Figure 21. Because of the divergence in solution near the wall for temperature, more work needs to be done for meshing near the wall to capture the steep temperature jump.

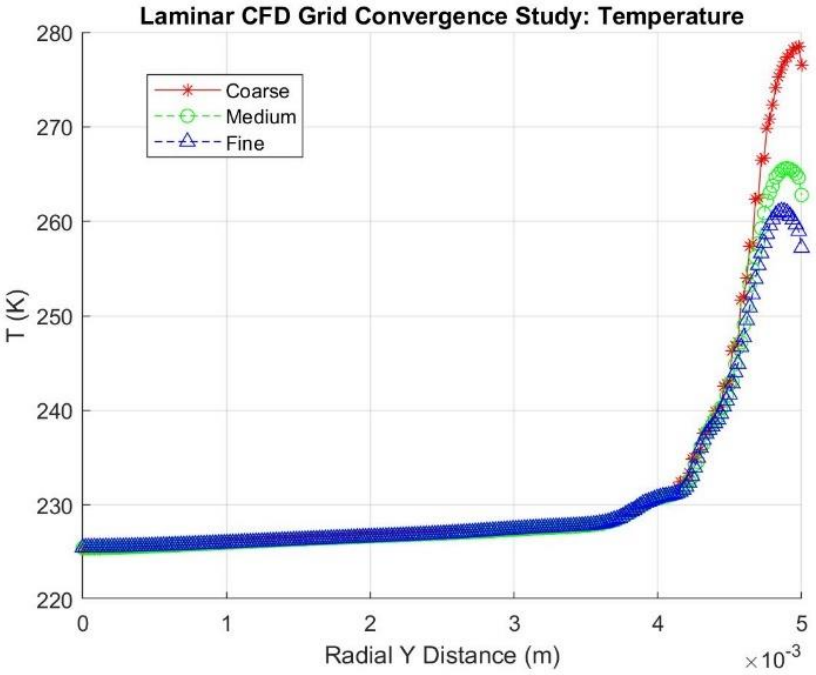

Figure 20: CFD Grid Convergence Study: Temperature

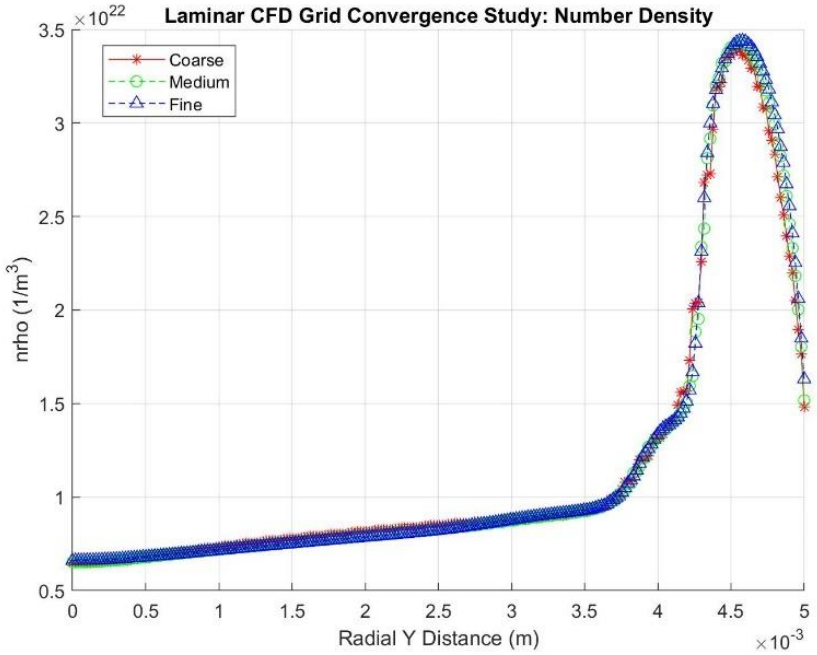

Figure 21: CFD Grid Convergence Study: Number Density

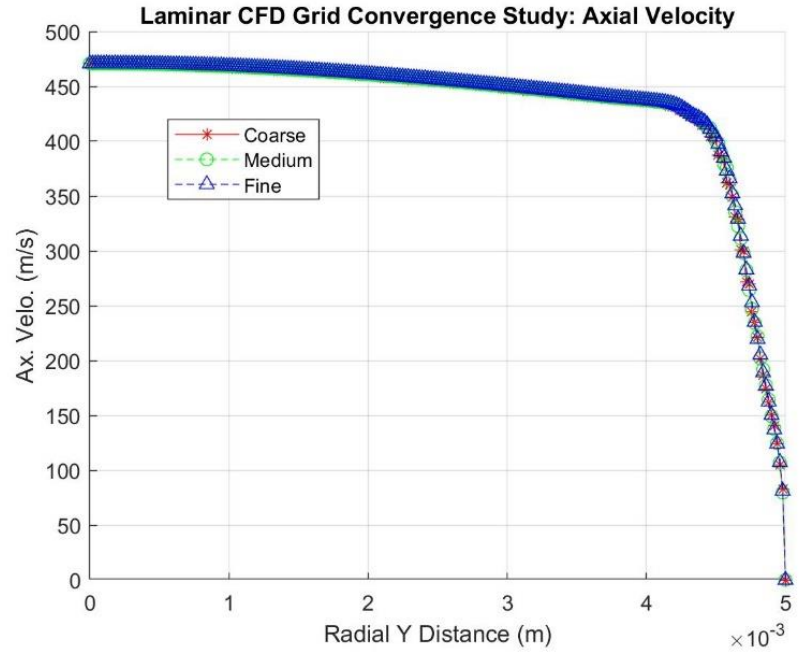

Figure 22: CFD Grid Convergence Study: Axial Velocity

The final timesteps for the residual plot of the fine mesh is shown in Figure 23. The residuals are all <1E-5 and show aqeuate convergence.

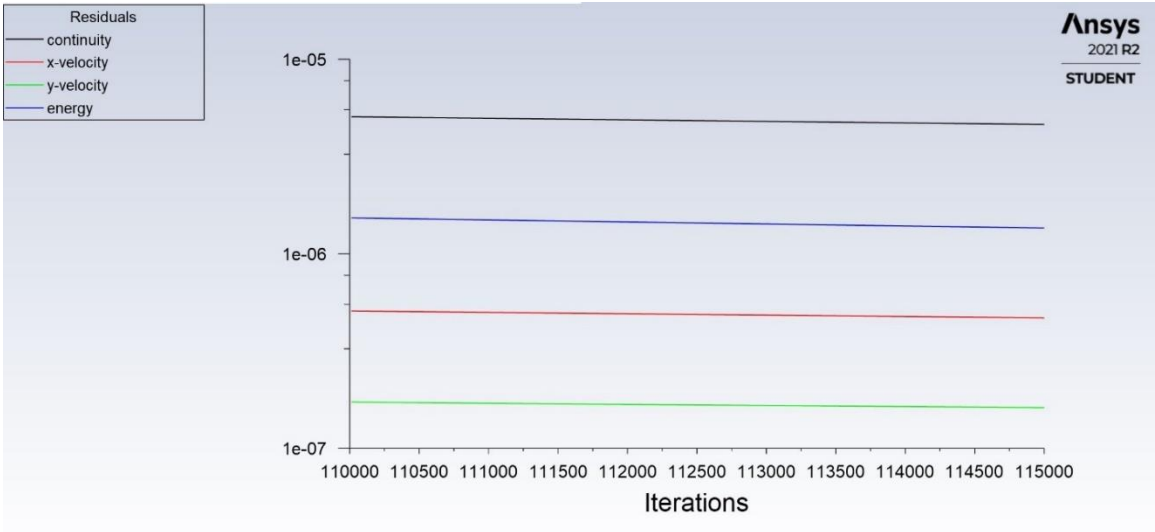

Figure 23: Iterative Convergence of Fine Mesh, Final Residuals

The final Non-Uniform inputs acquired are shown in Figures 24, 25, and 26. The full 2D exit profile for the values at the nozzle exit is shown for use in the DSMC test case. The temperature peaks near the adiabatic wall (the heat cannot be diffused), the velocity at the walls goes to zero (no-slip), and the number density drops accordingly.

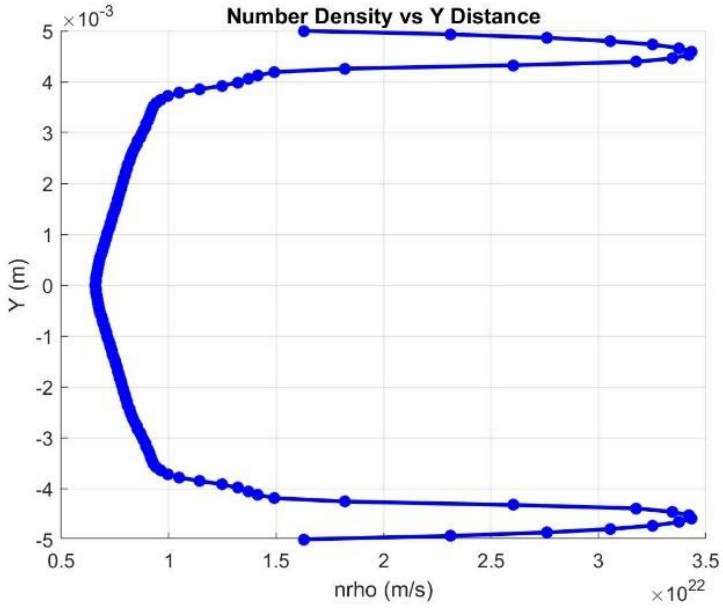

Figure 24: Non-Uniform CFD-Based Input for DSMC Nozzle Exit Conditions: nrho

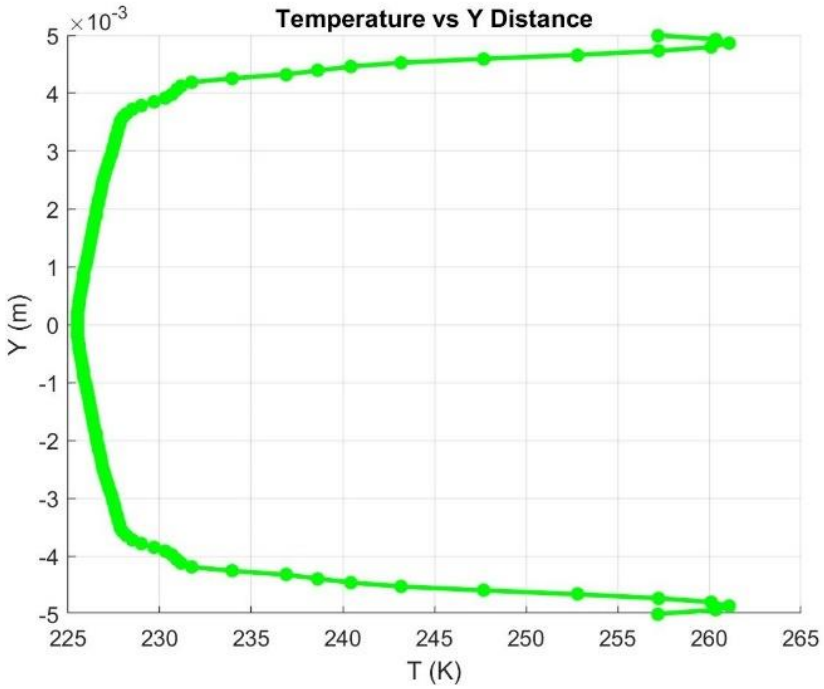

Figure 25: Non-Uniform CFD-Based Input for DSMC Nozzle Exit Conditions: T

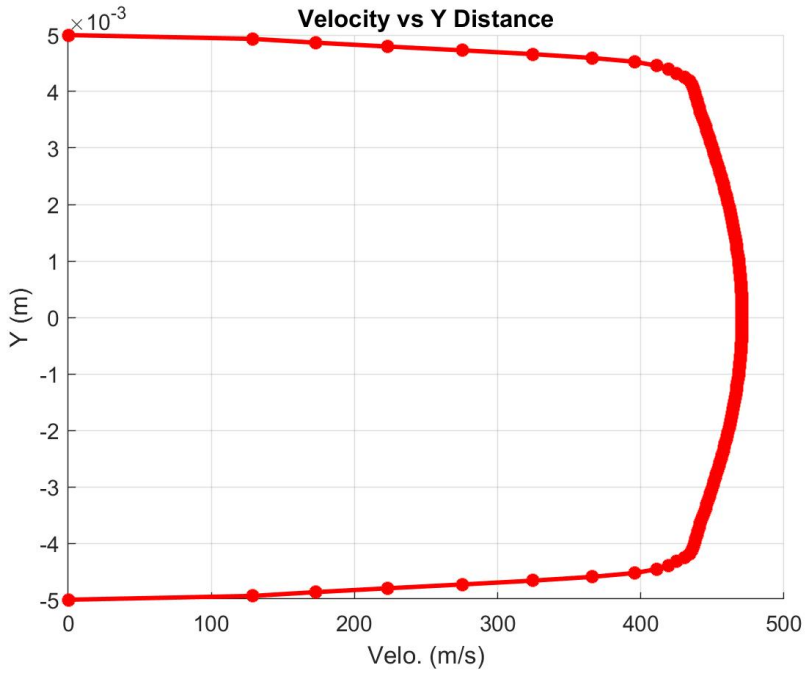

Figure 26: Non-Uniform CFD-Based Input for DSMC Nozzle Exit Conditions: Velocity

8.3 DSMC: Non-Uniform Input vs. Uniform Input compared to Plume Models

Figure 27 to Figure 29 shows a grid sensitivity study was done for both the uniform and non-uniform CFD-based input. Work must be done in certain regions for convergence of large gradients around x=.005 m for the non-uniform input. These solutions show that this large gradient could be caused by a shock at x=.005 m as there is a temperature and density spike there. The uniform input behaves as expected. It stays constant for a period then decreases both in temperature and density.

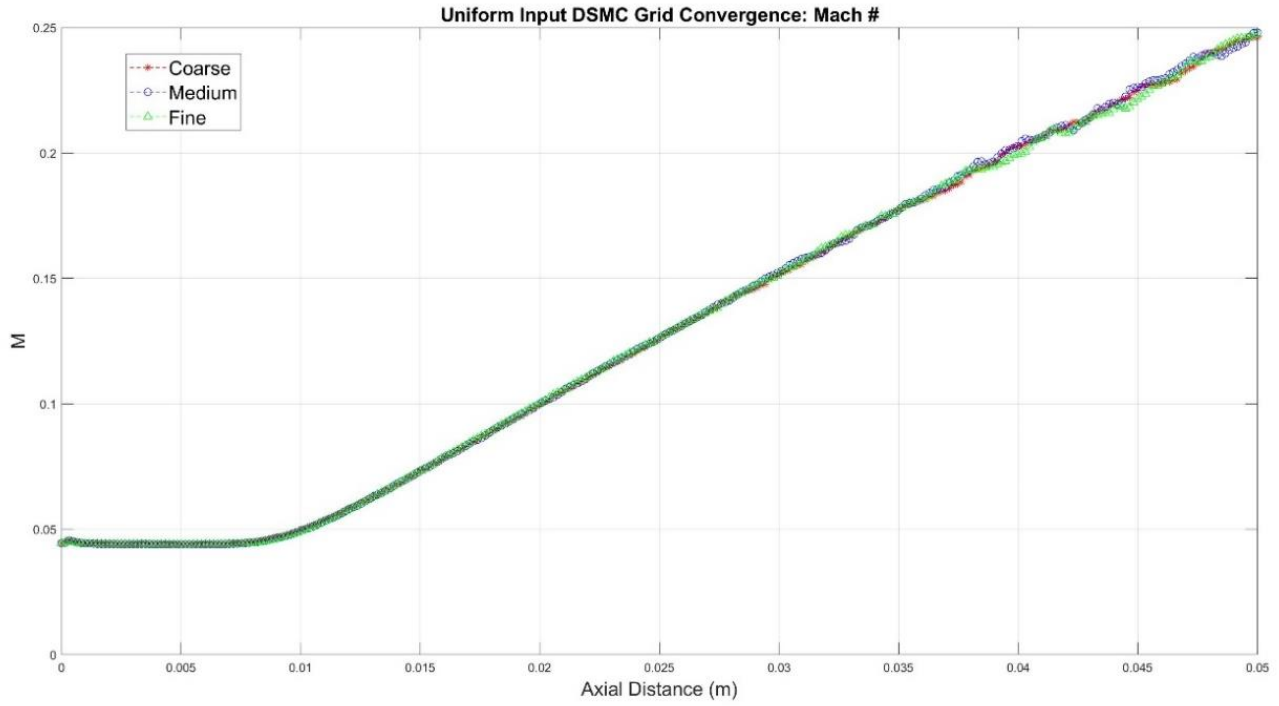

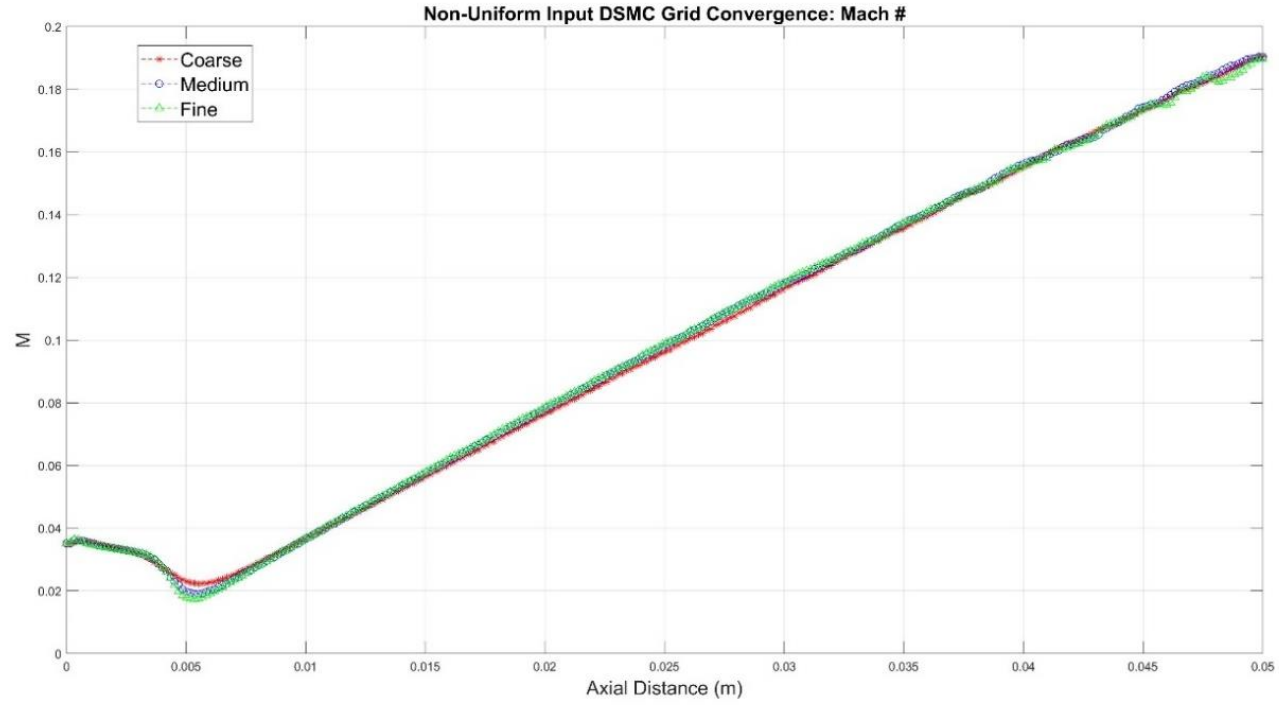

Figure 27: DSMC Grid Convergence Mach # a) Uniform b) Non-Uniform

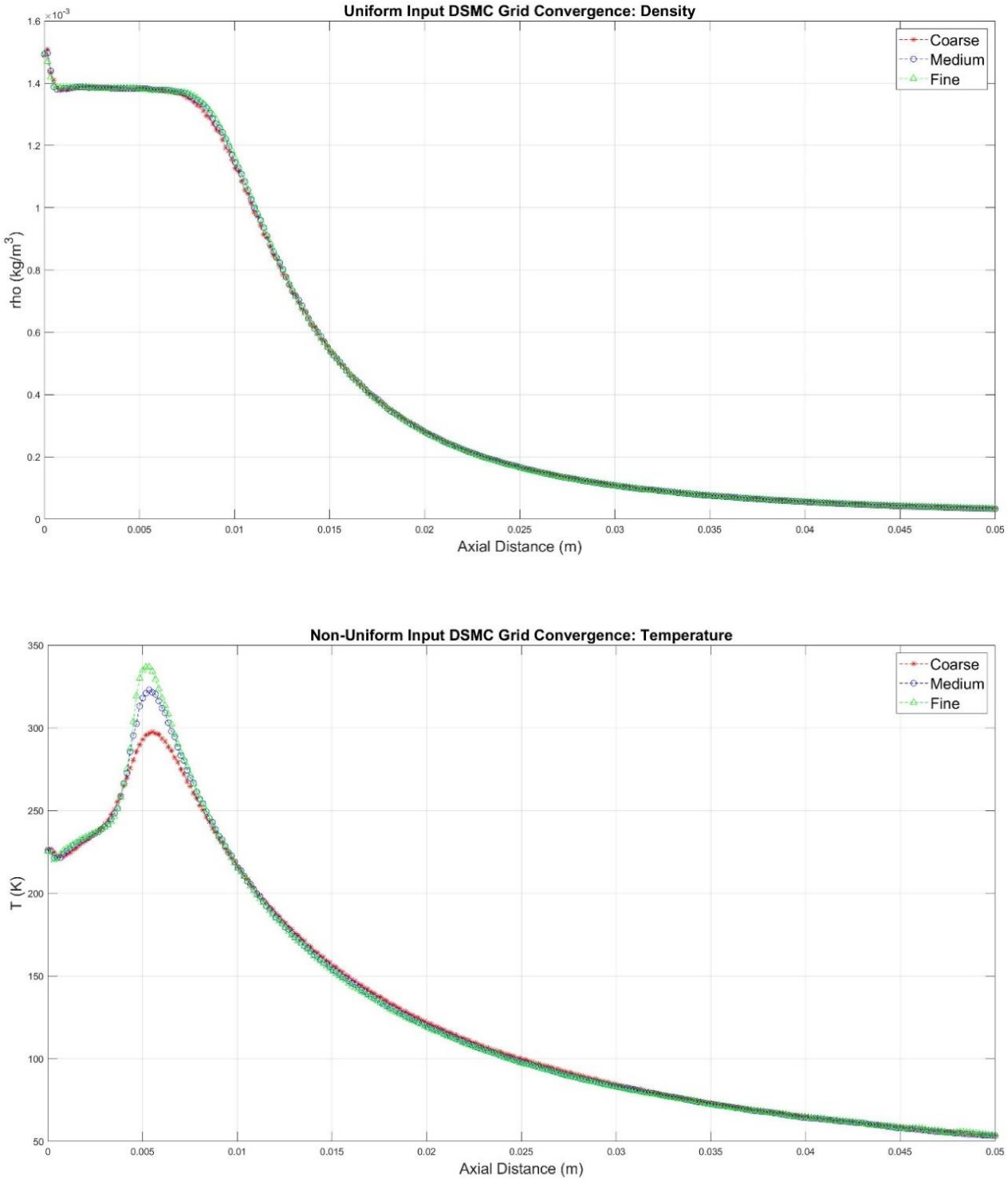

Figure 28: DSMC Grid Convergence Density a) Uniform b) Non-Uniform

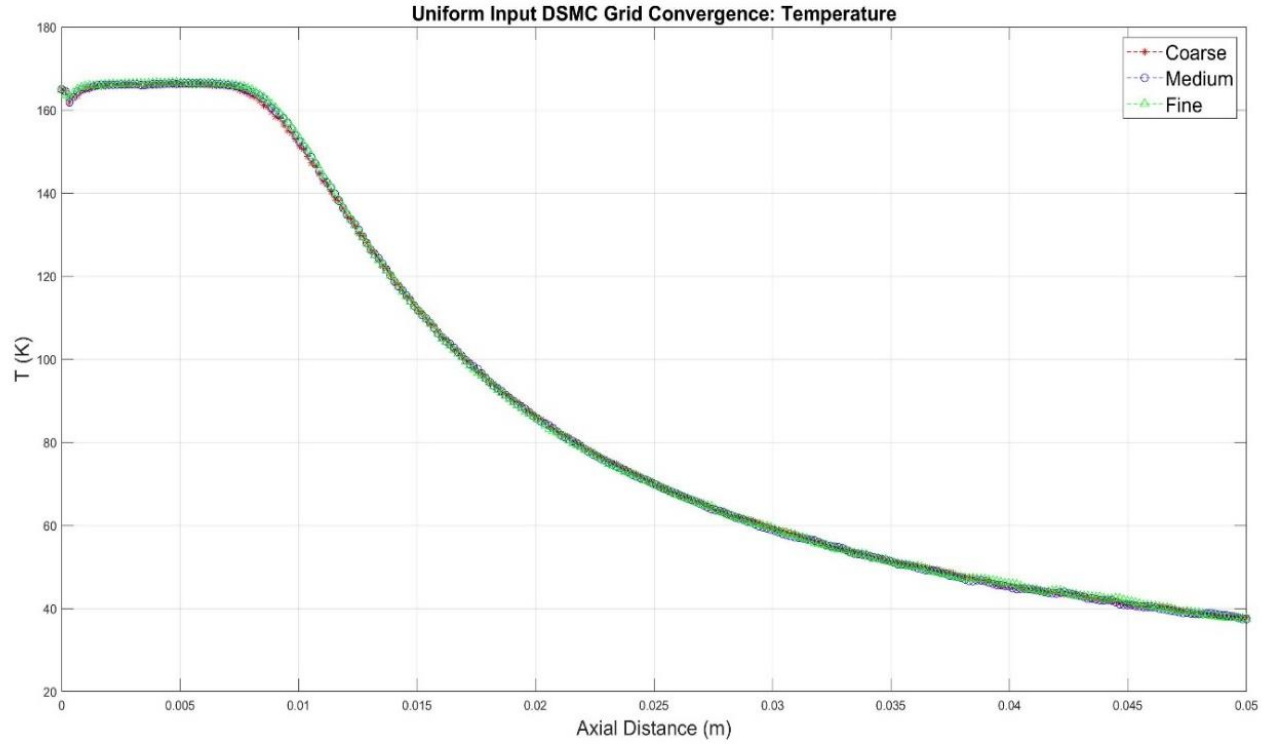

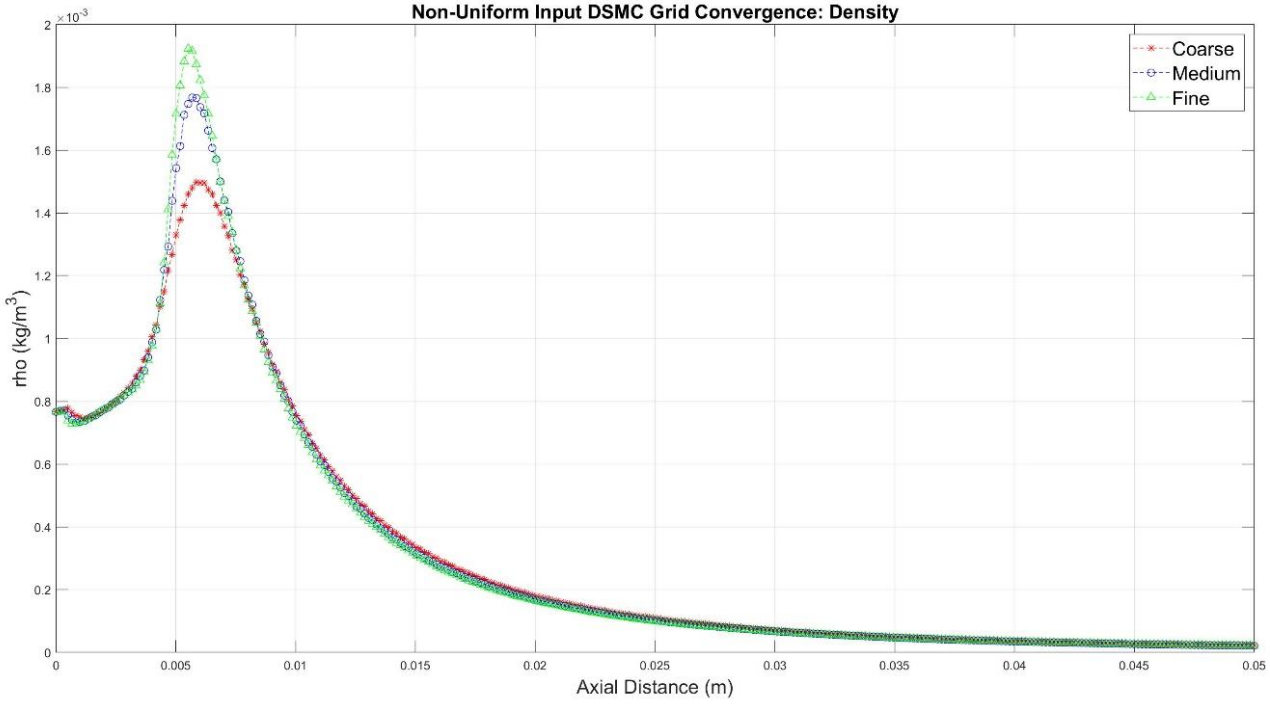

Figure 29: DSMC Grid Convergence Temperature a) Uniform b) Non-Uniform

Centerline values for the uniform and non-uniform plumes are compared in Figures 30-31. It can be seen that there is non-isentropic behavior occurring within the nozzle in Fluent which explains why the plumes differ. The uniform input assumed To=298 K. For the non-uniform input, To=~286 by the time the flow reaches the exit. This makes sense as there is a possible visible shock near x=.005m as there is a temperature and density spike.

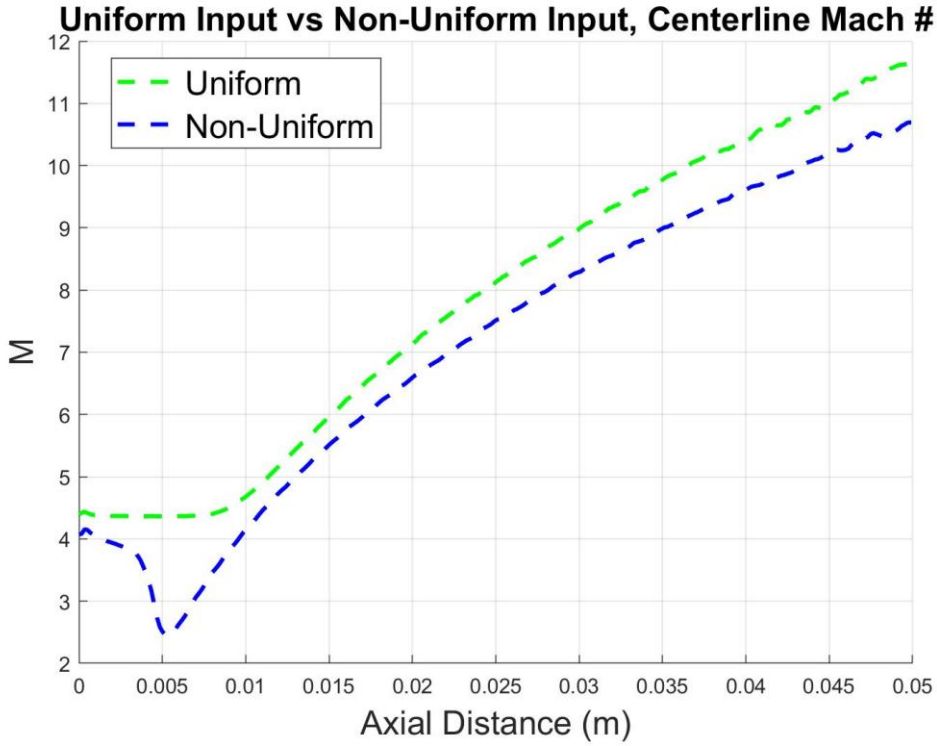

Figure 30: Uniform vs Non-Uniform Centerline Value Comparison: Mach #

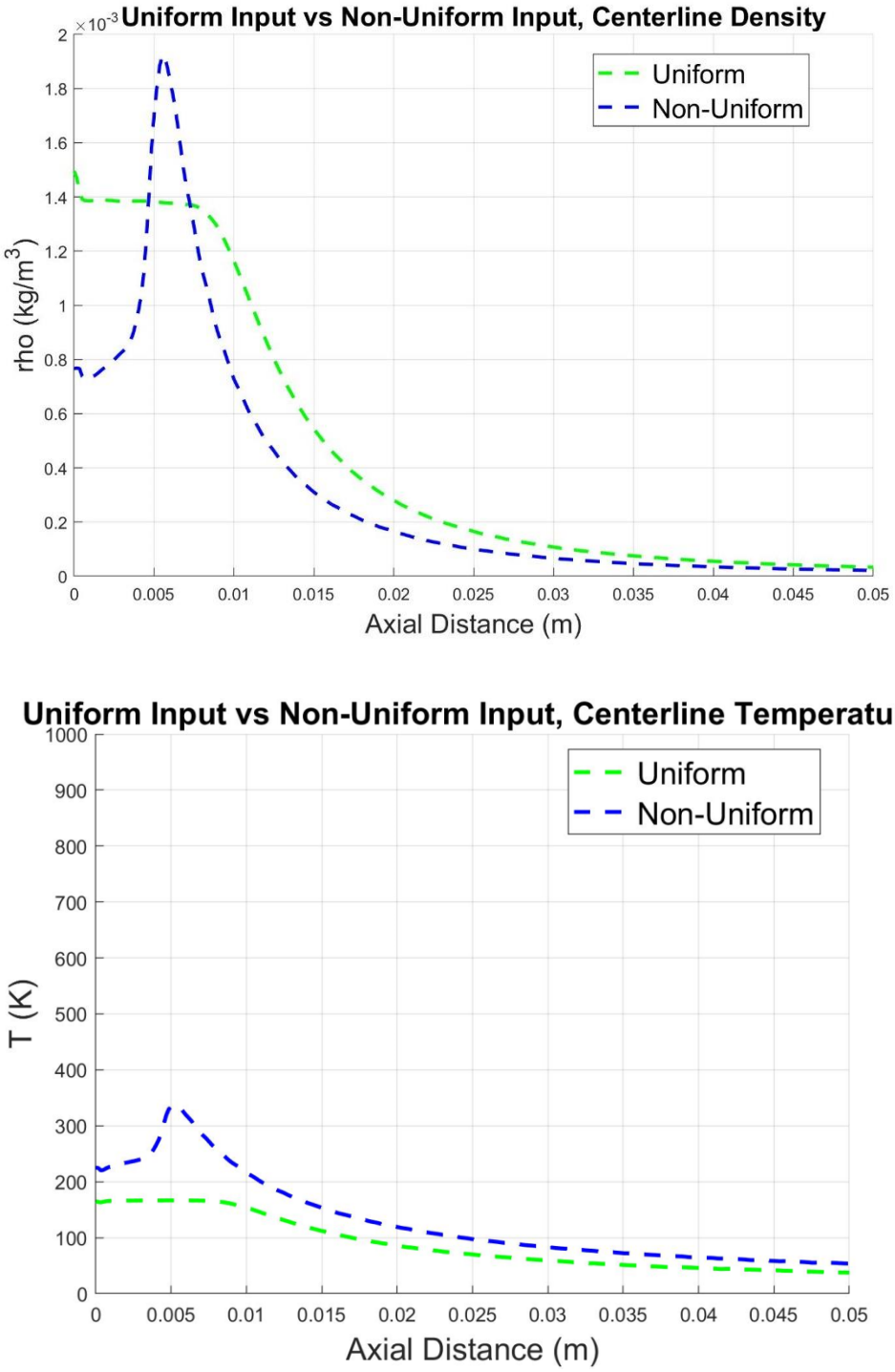

Figure 31: Uniform vs Non-Uniform Centerline Value Comparison: a) Density, b) Temperature

Lastly, Figures 32, 33, and 34 show the contour plots and Figure 32 shows the centerline plume values comparing each input to the models. From these plots, the Gerasimov model (Figure 29) describes the plume the best for both the uniform and non-uniform input as opposed to the Roberts-South and Simons-Boynton contour plots in Figures 33 and 34. The close convergence in the far-field is evident. This could be because the Gerasimov model's assumptions are very easily met for both inputs which give a supersonic, ideal gas plume. The results were not expected to be accurate in the near-field due to the point-source assumption which causes a singularity there.

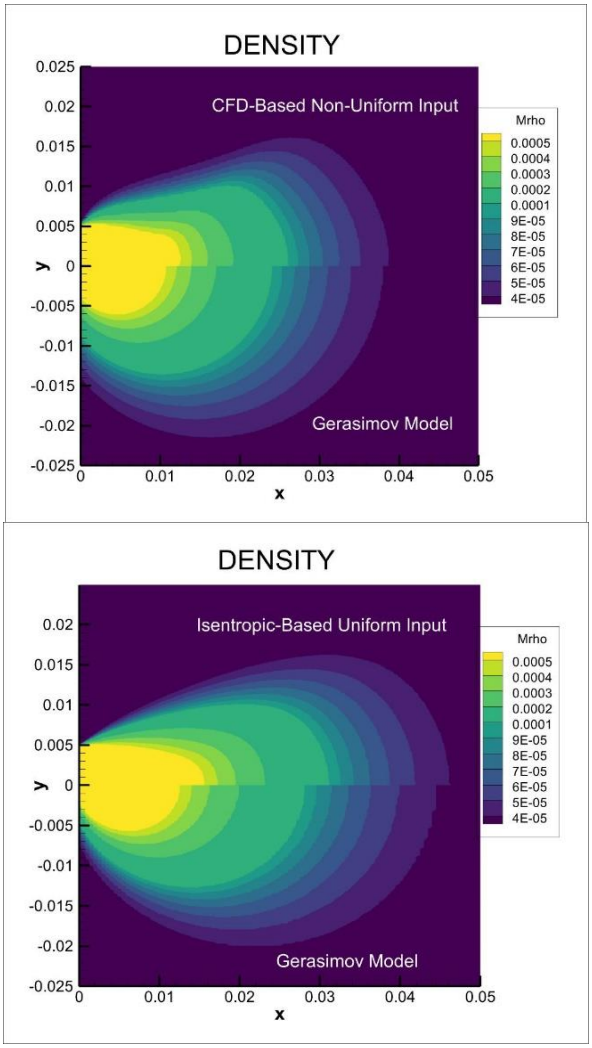

Figure 32: Density Contour Plot Comparison, Gerasimov plume model: a)Non-Uni, b)Uni

The Roberts and South Model has difficulty matching the DSMC plumes at large angles which can be seen in Figure 33. It also does not adequately model the non-uniform input which

can be seen by the lack of convergence in the far-field. Convergence of the uniform input is visually better than the convergence of the non-uniform input. The model's assumptions include that the flow is isentropic when it leaves the nozzle. The non-uniform input came from a simulation that had non-sentropic behavior within the nozzle and most likely left the nozzle as non-isentropic. This was evidenced by the large variable gradients discovered during the grid sensitivity study as well as the possible shock near x=.005m and explains the lack of convergence between the model plume and the DSMC plume even in the far-field.

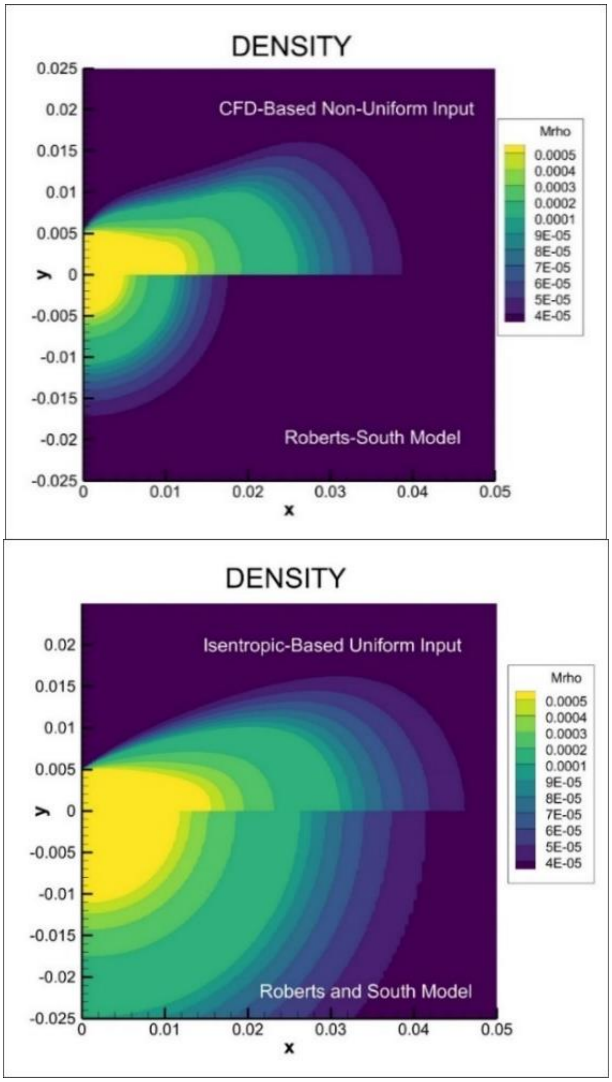

Figure 33: Density Contour Plot Comparison, Roberts & South plume model: a)Non-Uni, b)Uni

In contrast, the Simons-Boynton model is not adequate to model the uniform plume which can be seen by the lack of convergence in the far-field in Figure 34. However, it simulated

the non-uniform plume adequately as evidenced by the far-field convergence. The assumptions of this model mention that the model input is taken from the viscous layer. This means the model likely expects the plume it is in comparison with to be from a non-uniform input which explains why it models the uniform input so poorly.

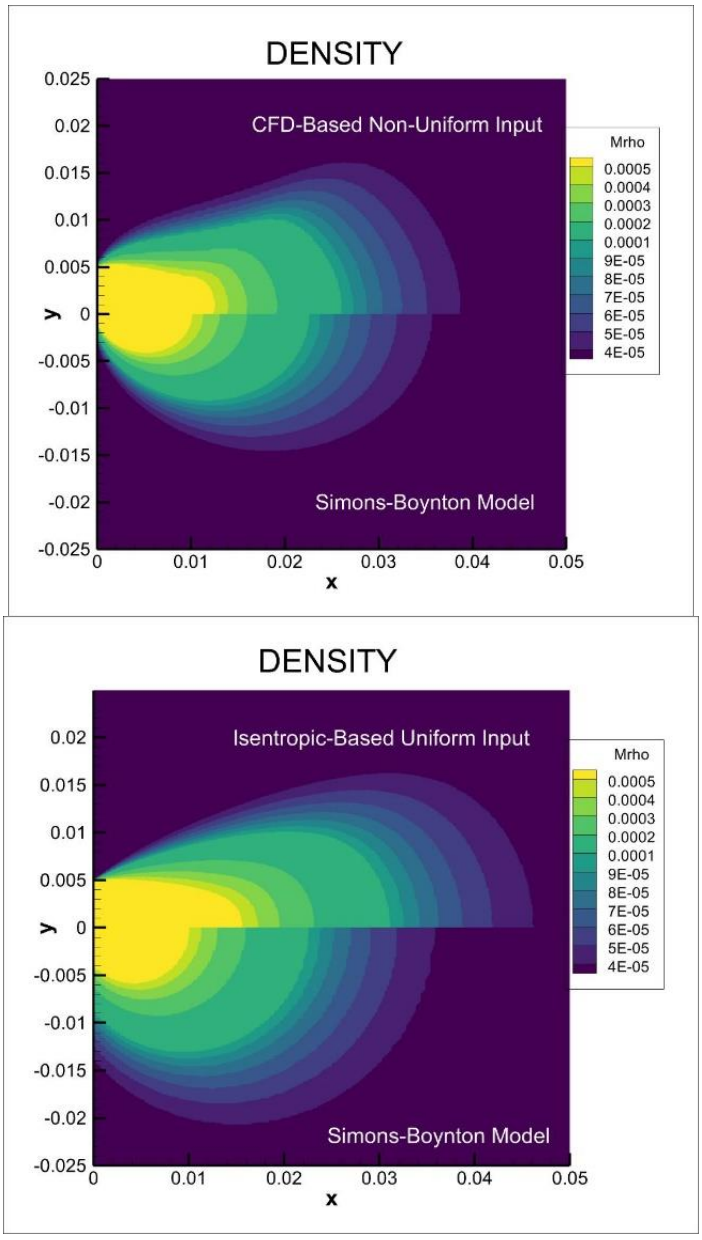

Figure 34: Density Contour Plot Comparison, Simons-Boynton plume model: a)Non-Uni, b)Uni

Figure 35 quantifies the values at the centerlines of the plume. Easily, it can be seen that the Gerasimov model describes the actual plume the best for both types of inputs.

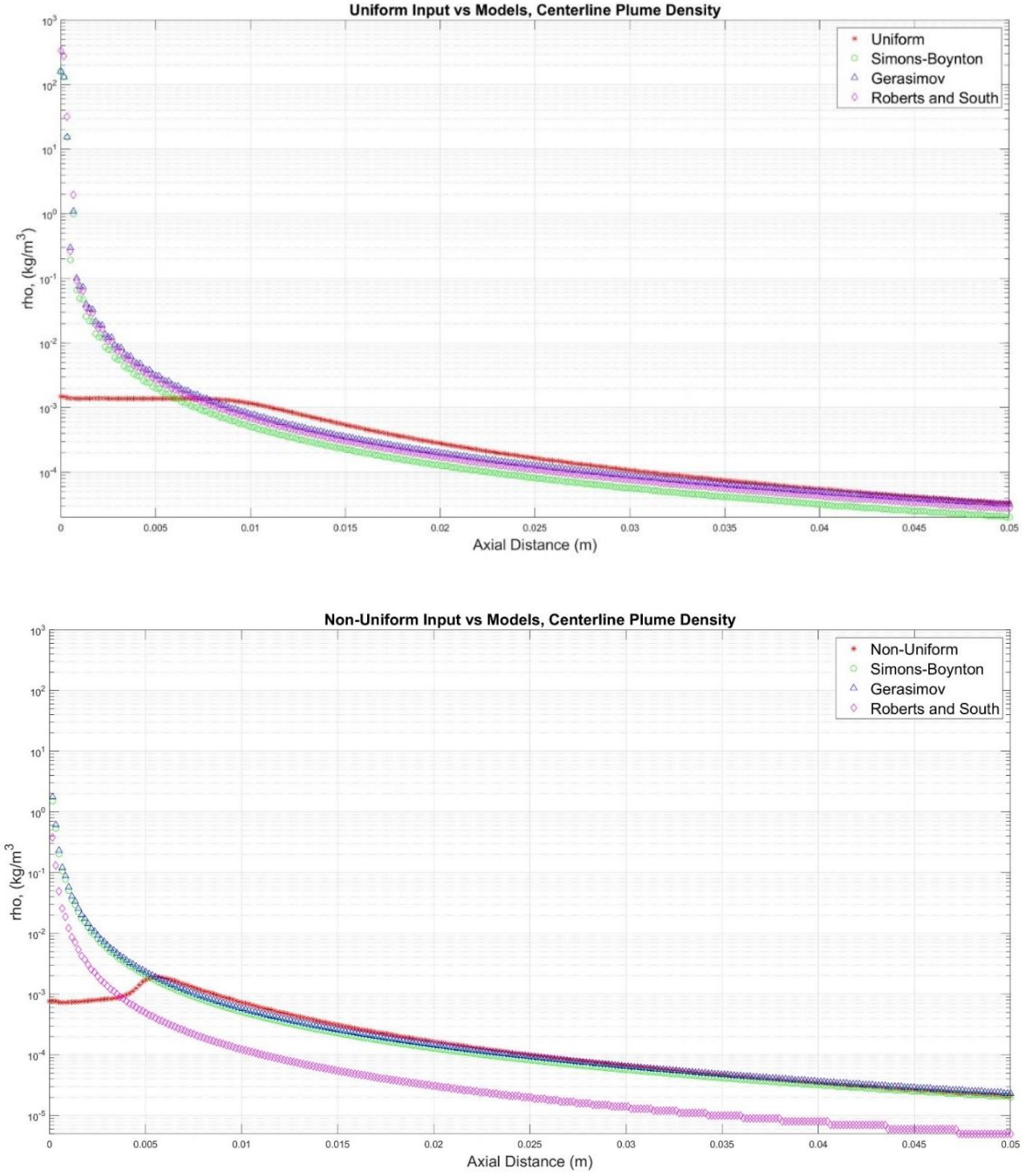

Figure 35: Density Along Plume Axis Comparison a)Uni, b)Non-Uni

8.4 Freestream Density Analysis

To see how the plume diffuses over a distance, the centerline densities of the uniform and non-uniform input plumes was normalized by the freestream density of 2.7765E-13 kg/m^3 for an altitude of 500 km (Figure 36). The freestream density equals the plume centerline density at .02 m for the uniform plume and .016 m for the non-uniform plume. It is apparent that the plume will not have a major effect on the cubesat 40 meters away from these results because it diffuses quickly in a perfect vacuum. Future work will assign the domain an atmospheric pressure for the inputs to diffuse into to analyze further.

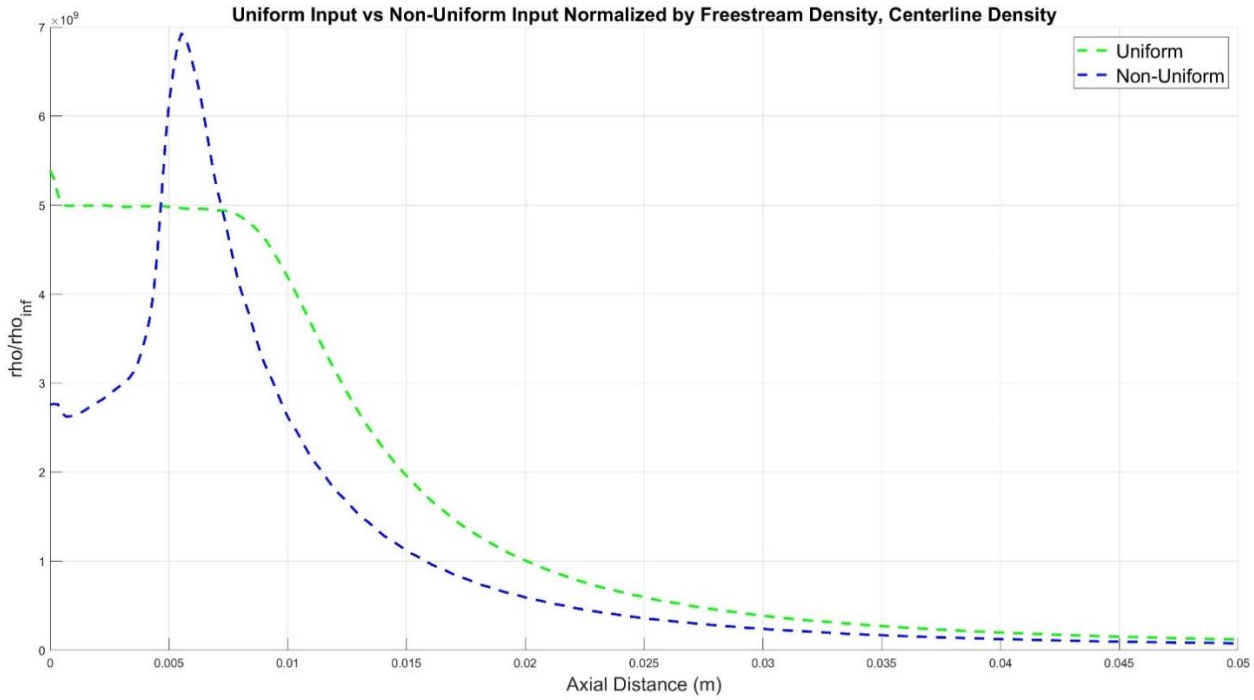

Figure 36: DSMC Plume Centerline Densities Normalized by Freestream Density at 500 km

8.5 DSMC and CFD Domain Parameters

Along with the DSMC plume contour plots in Figures 32-34 for the uniform and non-uniform inputs, the domain for the Mach number as well as Temperature is shown in Figures 37 and 38. It appears that around x=.005 there is a discontinuity for the non-uniform input while the uniform input has no discontinuities there. It is a sharp temperature rise and gas density increase which leads one to believe that there may be an oblique shock wave there as shown in Figure 32.

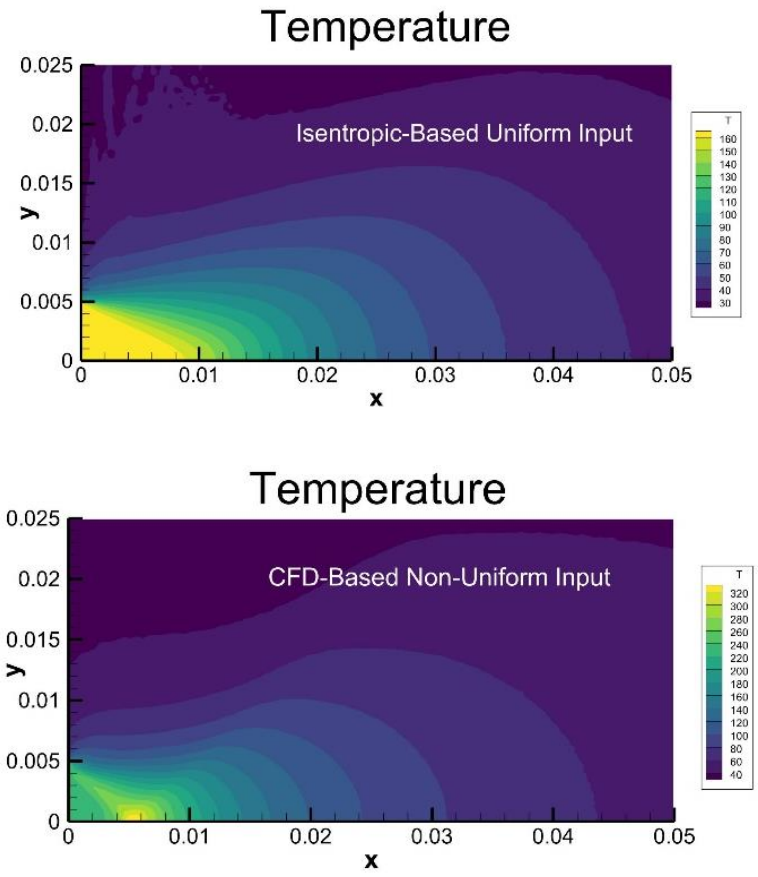

Figure 37: DSMC Domain Temperature a) Uni, b) Non-Uni

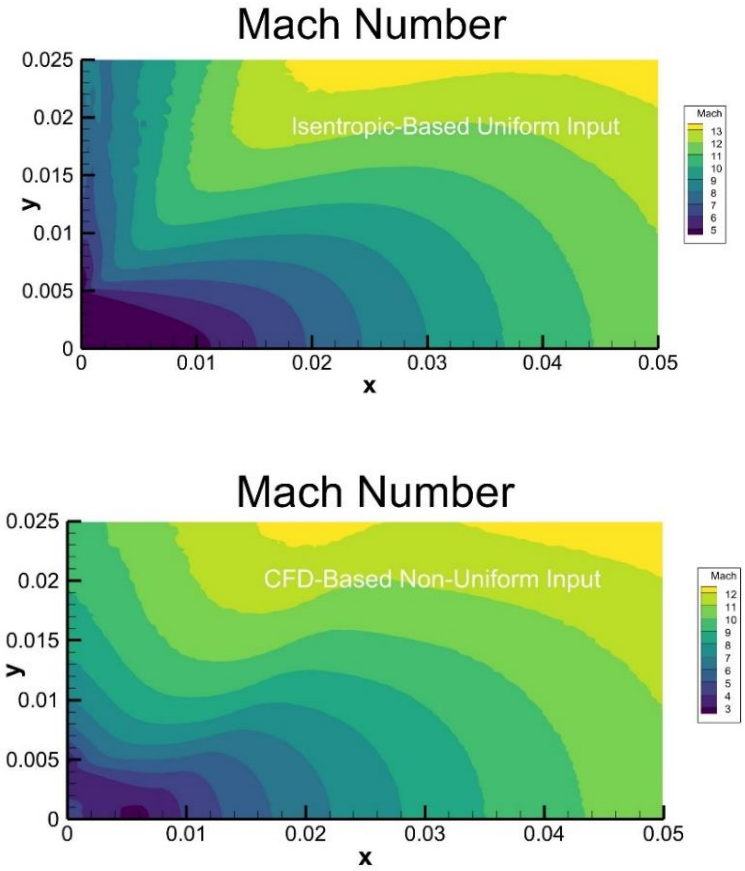

Figure 38: DSMC Domain Mach Number a) Uni, b) Non-Uni

The domains for the CFD simulation are given by Figures 39-42. It is clear from these contour plots that To does not stay as 298 from the throat of the nozzle to the exit signifying that the flow has some sort of non-isentropic behavior (Figure 40). Conditions at the pressure-outlet are supersonic as shown by the Mach number (Figure 41).

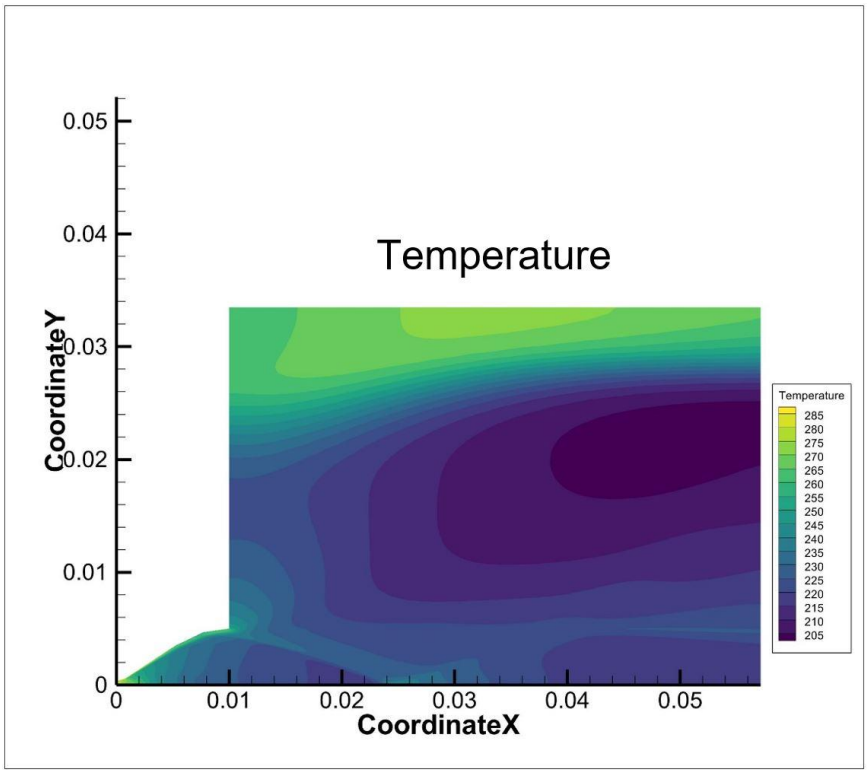

Figure 39: CFD Domain, Temperature

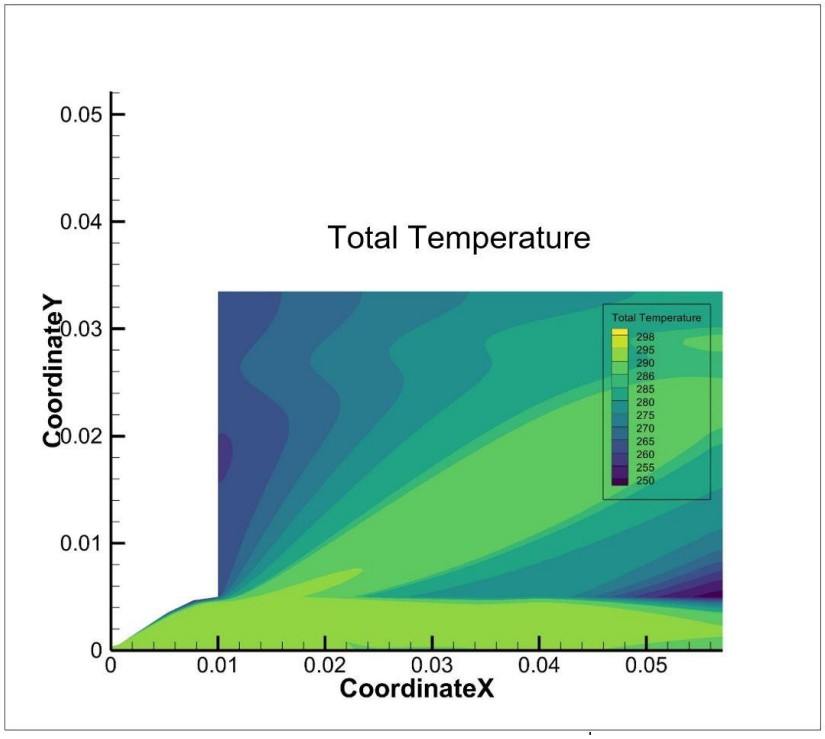

Figure 40: CFD Domain, Temperature

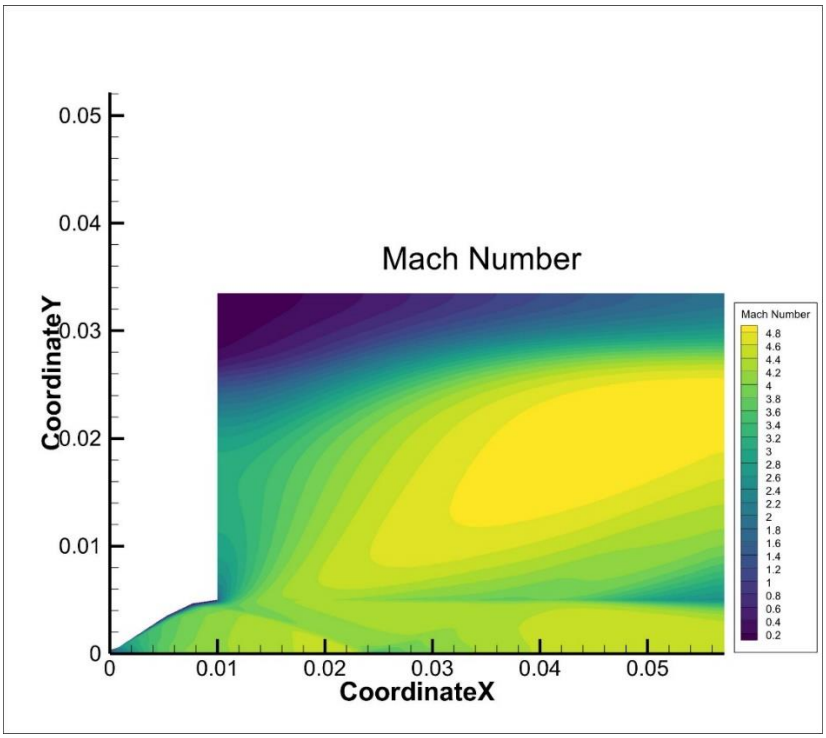

Figure 41: CFD Domain, Mach Number

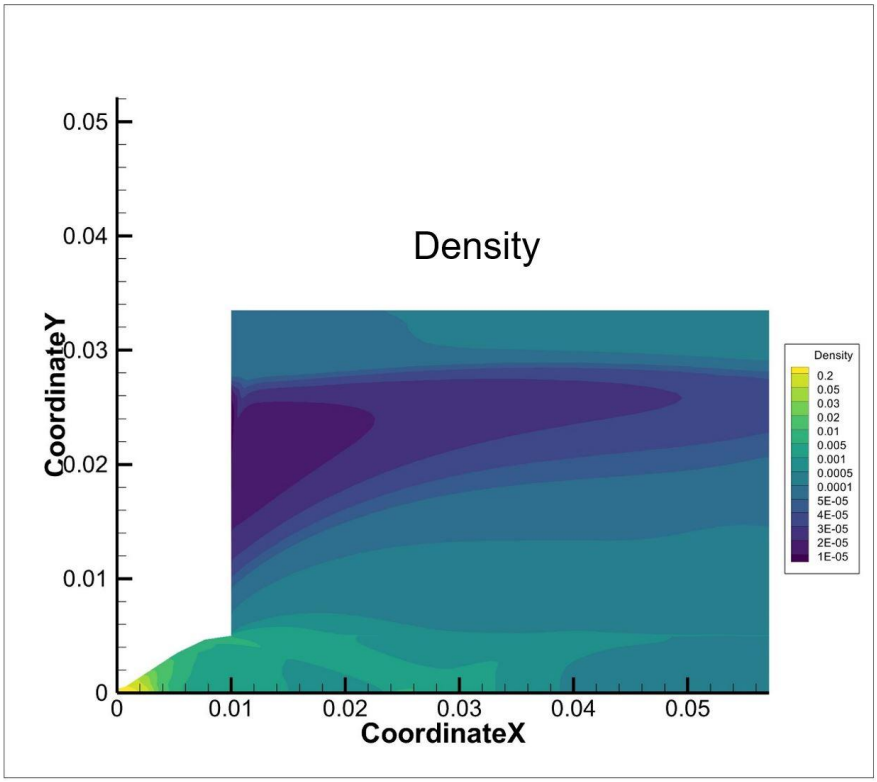

Figure 42: CFD Domain, Density

9. CONCLUSIONS AND FUTURE WORK

The influence from the nozzle walls is substantial and cannot be ignored. It makes a noticeable difference in each of the DSMC plumes. CFD should be used to acquire the inputs for future DSMC simulations. It was found that the Gerasimov model should be used as a starting point to form a correlation for the nozzle plume due to how robust it is for this system. It appears that the dense plume would not be a huge concern at 40 m due to how quickly it diffuses into a vacuum. Additionally, there appears to be a shock outside the nozzle for the non-isentropic plume causing non-isentropic behavior.

More work must be done examining flow fields obtained from both the DSMC and CFD simulations to analyze the behavior and improve upon boundary conditions. For DSMC, this would be the inclusion of an atmospheric pressure. For CFD, this would be the possible reconsidering of the outlet boundary conditions due to the flow's supersonic nature [35]. Depending on the flow, only certain boundary conditions can be specified in CFD. This topic will have to revisited later after further reading [35]. Additionally, the CFD mesh and DSMC grid regions that are not as converged must be refined where the discontinuity is located.

A correlation will be formed for the VISORS nozzle using insight about the analytical plume models to describe the plume efficiently. This correlation will be confirmed by inputting a variety of thrust levels into it to compare to DSMC results. Close range plume impingement from other nozzles on the CubeSat will be analyzed where flow issues at an angle using this correlation.

REFERENCES

[1] A. R. Gundamraj, R. Thatavarthi, C. A. Carter, E. G. Lightsey, A. W. Koenig, and S. D'amico, "Preliminary design of a distributed telescope cubesat formation for coronal observations," AIAA Scitech 2021 Forum, no. January, pp. 1–16, 2021, doi: 10.2514/6.2021-0422.

[2] Private Communication with Arun Chinnapan

[3] Thomson, A., "High, altitude rocket plume structure," General Dynamics Convair Rept. GDC-DBE65-023 (September 1965).

[4] F. P. Boynton, "Highly underexpanded jet structure - Exact and approximate calculations," AIAA Journal, vol. 5, no. 9, pp. 1703–1704, 1967, doi: 10.2514/3.4283.

[5] F. P. Boynton, "Exhaust plumes from nozzles with wall boundary layers," Journal of Spacecraft and Rockets, vol. 5, no. 10, pp. 1143–1147, 1968, doi: 10.2514/3.29439.

[6] G. A. Simons, "Effect of nozzle boundary layers on rocket exhaust plumes," AIAA Journal, vol. 10, no. 11, pp. 1534–1535, 1972, doi: 10.2514/3.6656.

[7] J. E. Vesper, T. J. M. Broeders, J. Batenburg, D. E. A. van Odyck, and C. R. Kleijn, "The interaction of parallel and inclined planar rarefied sonic plumes—From free molecular to continuum regime," Physics of Fluids, vol. 33, no. 8, pp. 1–23, 2021, doi: 10.1063/5.0056730.]

[8] G. A. Simons, "Effect of nozzle boundary layers on rocket exhaust plumes," AIAA Journal, vol. 10, no. 11, pp. 1534–1535, 1972, doi: 10.2514/3.6656.

[9] J. E. Vesper, T. J. M. Broeders, J. Batenburg, D. E. A. van Odyck, and C. R. Kleijn, "The interaction of parallel and inclined planar rarefied sonic plumes—From free molecular to continuum regime," Physics of Fluids, vol. 33, no. 8, pp. 1–23, 2021, doi: 10.1063/5.0056730.]

[10] L. Roberts and J. C. South, "Comments on exhaust flow field and surface impingement," AIAA Journal, vol. 2, no. 5, pp. 971–973, 1964, doi: 10.2514/3.2443.

[11] Roberts, L , Exhaust jet dust layer interaction during a lunar landing " Thirteenth International Astronautical Congress, Varna, Bulgaria (September 23-29, 1962)

[12] M. S. Ivanov, G. N. Markelov, Y. I. Gerasimov, A. N. Krylov, L. v. Mishina, and E. I. Sokolov, “Free-flight experiment and numerical simulation for cold thruster plume,” Journal of Propulsion and Power, vol. 15, no. 3, pp. 417–423, 1999, doi: 10.2514/2.5460.

[13] Gerasimov, Y. I., “Similarity Parameters in the Problem of Interaction of a Free Expanding Jet with a Plate,” Izvestiya Akademii Nauk SSSR, Seriya Mekhanika Zhidkosti i Gaza (translated as Fluid Dynamics), Vol. 2, No. 2, 1981, pp. 169–173.

[14] Герасимов Ю И, Ярыгин В Н, Крылов А Н, Сагдуллин, Б А Моделирование структуры течения в составной струе за двумя двигателями , расположенными около корпуса космического аппарата, 2009, pages 395-404

[15] Image, https://www.researchgate.net/publication/235898245_A_Review_of_Acoustic_Absorption_Mechanisms_of_Nanoscopic_Fibres/figures?lo=1

[16] A. A. Alexeenko and S. F. Gimelshein, “Direct simulation monte carlo,” Handbook of Fluid Dynamics: Second Edition, pp. 39.1-39.40, 2016, doi: 10.1201/b19031-45.

[17] Kepmenkes Keselamatan Pasien Rumah Sakit, “Quantification of Modeling Uncertainties in Hypersonic Non-Equilibrium Flows, 2011.

[18] G. A. Bird, Molecular Gas Dynamics and the Direct Simulation of Gas Flows. Oxford University Press, 1994.

[19] A. Venkattraman, A. A. Alexeenko, M. A. Gallis, and M. S. Ivanov, “A comparative study of no-time-counter and majorant collision frequency numerical schemes in DSMC,” AIP Conference Proceedings, vol. 1501, no. 1, pp. 489–495, 2012, doi: 10.1063/1.4769577

[20] Aaron Pikus, https://www.youtube.com/watch?v=cSFr8MTr30Y

[21] Image, https://brilliant.org/wiki/cylindrical-coordinates/

[22] Climalife Physical Properties of R236-fa Handout

[23] Shen, V.K., Siderius, D.W., Krekelberg, W.P., and Hatch, H.W., Eds., NIST Standard Reference Simulation Website, NIST Standard Reference Database Number 173, National Institute of Standards and Technology, Gaithersburg MD, 20899, http://doi.org/10.18434/T4M88Q

[24] Arun Chinnapan’s previous IQmol calculations of HFC

[25] Outcalt, S.L.; McLinden, M.O., An equation of state for the thermodynamic properties of R236fa, NIST report to sponsor (U.S. Navy, David Taylor Model Basin) under contract N61533-94-F-0152, NIST, Gaithersburg, MD, 1995, 0.

[26]Laesecke, A.; Defibaugh, D.R., Viscosity of 1,1,1,2,3,3-hexafluoropropane and 1,1,1,3,3,3-hexafluoropropane at saturated-liquid conditions from 262K to 353K, J. Chem. Eng. Data, 1996, 41, 1, 59-62

[27] Geller, V.; Bivens, D.B.; Yokozeki, A., Transport properties and surface tension of hydrofluorocarbons HFC236fa and HFC245fa, Proc. 20th Int. Congress of Refrig, IIR/IIF, Sydney, Australia, 1999

[28] Private Communication with Petr Kazarin

[29] Marcia L. Huber, Arno Laesecke, and Richard A. Perkins, Industrial & Engineering Chemistry Research 2003 42 (13), 3163-3178, DOI: 10.1021/ie0300880

[30] Image, http://www.coolprop.org/fluid_properties/fluids/R236FA.html

[31] Private Communication with Sam Hart, Georgia Tech.

[32] Nadia Numa, Arun Chinnappan, Alina Alexeenko, Adam W. Koenig, and Simone D'Amico, "Analysis of Effects of Atmospheric Drag on the VISORS Mission," 2020.

[33] Private Communication with Prof. Shih and Sabina Nketia

[34] https://byjus.com/chemistry/degree-of-freedom/

[35] AAE 512 Notes

[36] https://sparta.github.io/

[37] Principles of Fermentation Technology (Third Edition), 2017